

# Multi-Modal Explainable Medical AI Assistant for Trustworthy Human-AI Collaboration

Honglong Yang<sup>1</sup>, Shanshan Song<sup>1</sup>, Yi Qin<sup>1</sup>, Lehan Wang<sup>1</sup>, Haonan Wang<sup>1</sup>,  
Xinpeng Ding<sup>1</sup>, Qixiang Zhang<sup>1</sup>, Bodong Du<sup>1</sup>, Xiaomeng Li<sup>1,2\*</sup>

<sup>1</sup>Department of Electronic and Computer Engineering,  
The Hong Kong University of Science and Technology

<sup>2</sup>Department of Computer Science and Engineering,  
The Hong Kong University of Science and Technology

## Abstract

Generalist Medical AI (GMAI) systems have demonstrated expert-level performance in biomedical perception tasks, yet their clinical utility remains limited by inadequate multi-modal explainability and suboptimal prognostic capabilities. Here, we present XMedGPT, a clinician-centric, multi-modal AI assistant that integrates textual and visual interpretability to support transparent and trustworthy medical decision-making. XMedGPT not only produces accurate diagnostic and descriptive outputs, but also grounds referenced anatomical sites within medical images, bridging critical gaps in interpretability and enhancing clinician usability. To mitigate overreliance and support real-world deployment, we introduce a reliability indexing mechanism that quantifies uncertainty through consistency-based assessment via interactive question-answering. We validate XMedGPT across four pillars: multi-modal interpretability, uncertainty quantification, and prognostic modeling, and rigorous benchmarking. The model achieves an Intersection over Union (IoU) of 0.703 across 141 anatomical regions, and a Kendall’s tau-b of 0.479 ( $P < 0.05$ ), demonstrating strong alignment between visual rationales and clinical outcomes. For uncertainty estimation, it attains an AUC of 0.862 on visual question answering and 0.764 on radiology report generation. Trained on over 7 million image-text pairs—including 1.6 million with pixel-level annotations—XMedGPT enables precise tumor morphology analysis and longitudinal change detection. In survival and recurrence prediction for lung and glioma cancers, it surpasses prior leading models by 26.9%, and outperforms GPT-4o by 25.0%. Rigorous benchmarking across 347 datasets covers 40 imaging modalities and external validation across four anatomical systems confirming exceptional generalizability, with performance gains surpassing existing GMAI by 20.7% for in-domain evaluation and 16.7% on 11,530 in-house data evaluation. Together, XMedGPT represents a significant leap forward in clinician-centric AI integration, offering trustworthy and scalable support for diverse healthcare applications.

## Introduction

Multimodal Large Language Models (MLLMs), trained on extensive and diverse datasets, have driven transformative advances in artificial intelligence [35, 54, 81, 56, 11] and catalyzed the development of Generalist Medical AI (GMAI) in healthcare. Unlike domain-specific foundation models [57, 87, 8, 95, 45, 13, 69] and pre-trained biomedical models [91, 93] that require extensive task-specific adaptation to perform downstream tasks, GMAI [91, 63, 84, 51, 29, 80] represents a multimodal,

\*Corresponding author: Xiaomeng Li (eexmli@ust.hk).

task-versatile system capable of integrating diverse medical modalities and generating outputs (e.g., interactive clinical guidance) to optimize healthcare delivery and enhance clinical decision-making. While MLLMs underpin these systems by integrating visual and textual biomedical data, their translation into trustworthy, clinician-ready tools remains insufficiently explored, primarily due to the following unresolved challenges.

First, existing GMAI systems lack multimodal explainability, which undermines their trustworthiness for use in clinical practice. Although these models can generate text-based outputs for diverse inputs, including medical images and clinician instructions, they may produce unreliable diagnostic conclusions without visual explainability pinpointing the precise locations of potential diseases and textual explainability to articulate diagnostic reasoning and quantify prediction confidence. This deficiency in multimodal interpretability can lead clinicians to inadvertently rely on unverified outputs without thoroughly cross-referencing them with the medical images and patient information, leading to potential misdiagnosis [46, 15, 42, 74, 75]. Second, existing GMAI systems are mainly

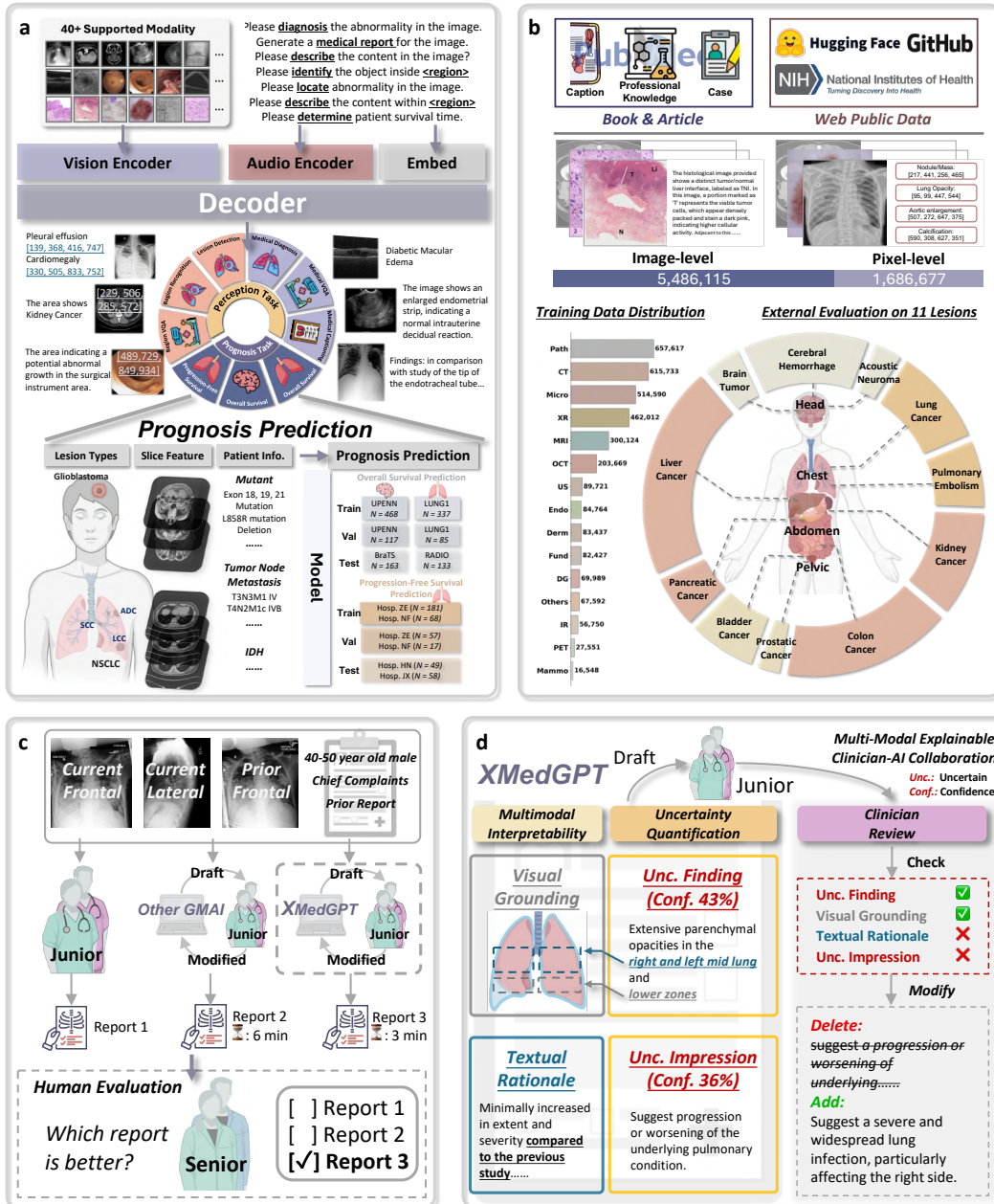




Figure 1: **a**, XMedGPT is a versatile multi-modal AI framework designed to handle over 40 distinct image modalities while seamlessly integrating inputs from images, text, audio. Beyond image-level perception tasks, it excels in pixel-level analysis alongside complex prognostic modeling, including overall and progression-free survival predictions. **b**, The training dataset consists of 7 million image-text, including 1.6 million with pixel-level annotations. External validation spans 11 lesion types across 4 anatomical regions, including the brain, lungs, abdomen, and pelvis. **c**, In the human-centric evaluation, senior clinicians blindly assessed three reports from (1) human-written, (2) junior clinician + baseline AI (GMAI), and (3) junior clinician + XMedGPT. Senior clinicians provided detailed feedback to identify the best approach. **d**, XMedGPT-clinician collaboration flow. The model drafts a report with multi-modal interpretability and a reliability index, which the clinician refines by verifying the provided evidence. This process enhances clinical decision-making by combining AI’s analytical power with clinician expertise.

limited to performing perception tasks, achieving performance comparable to that of clinicians. However, they lack the ability to learn from relationships among multiple medical images and to model complex dynamics, such as those involving multiple visits or longitudinal patient data. Consequently, these systems remain limited to perform advanced prognostic tasks, such as predicting treatment outcomes (e.g., survival or recurrence) which require integrating multi-source information like patient demographics, imaging biomarkers, and longitudinal disease progression. These tasks are challenging even for expert clinicians, who often struggle to consistently and accurately quantify patient risks [28, 21, 87, 1]. Third, prior work lacks rigorous external evaluation using real-world clinical data and is often limited to institution-specific tasks or narrow healthcare contexts.

Here, we propose XMedGPT, a clinician-centric, multi-modal explainable medical AI assistant that employs a unified framework to seamlessly integrates visual and textual explainability. XMedGPT not only generates accurate text outputs but also visually highlights the anatomical locations referenced in the text within medical images, effectively addressing critical gaps in interpretability and significantly enhancing clinical usability. To foster trustworthy human-AI collaboration, we introduce the Reliability Indexing mechanism, which assesses model uncertainty by evaluating the consistency of the system’s predictions through interactive question-and-answer interactions. Instead of relying solely on the initial output, which may be influenced by the model’s learned reliance on common reporting templates or structural conventions, XMedGPT breaks down the output into a series of related visual question-answering (VQA) pairs—addressing questions about the presence, location, and severity of lesions. The critical attributes in the sentence are then validated using these image-driven VQA responses. The reliability index is computed by measuring the entropy of the consistency distribution between the attributes extracted from the sentence and the corresponding image-based answers, classifying the results into three reliability levels—high, medium, or low. This approach allows clinicians to efficiently identify areas requiring further review, enhancing the trustworthiness and interpretability of the model’s outputs and fostering improved human-AI collaboration.

Our XMedGPT was trained on a large-scale biomedical image dataset, which includes over 7 million image-text pairs, including 1.6 million pairs with pixel-level annotations, spanning 40 medical modalities and 141 anatomical regions. This extensive training enables XMedGPT to conduct pixel-level analysis of tumor morphology and detect subtle longitudinal changes across multiple visits — critical factors for accurate prognostic modeling. We demonstrate that XMedGPT unlocks state-of-the-art accuracy in predicting critical outcomes such as survival and recurrence (Figure 1a) from high-incidence cancers (e.g., lung adenocarcinoma) to high-mortality diseases (e.g., glioblastoma). In predicting lung cancer progression-free survival (PFS), which requires integration of patient data from multiple visits, XMedGPT achieved an AUC of 0.725 (95% CI: 0.635–0.809). In comparison, previous leading model [18] attained an AUC of 0.625 (95% CI: 0.511–0.727), and GPT-4o [35] achieved an AUC of 0.620 (95% CI: 0.526–0.712). Additionally, for survival prediction in glioblastoma and non-small cell lung cancer (NSCLC) using single-visit data, XMedGPT consistently outperforms previous state-of-the-art model [69, 9] by 16.9% and GPT-4o [35] by 29.05%. On 23 public benchmarks, XMedGPT consistently outperformed previous state-of-the-art (SOTA) GMAI model [80] by 26.2% and surpassed GPT-4o by 29.1% across 18 biomedical tasks while achieving a 29.3% F1-score improvement in pixel-level lesion characterization over prior SOTA model [34]. In a rigorous external validation using real-world clinical data covering nine common cancers across four anatomical regions (head, chest, abdomen, and pelvis) and two

high-incidence lesions (cerebral hemorrhage and pulmonary embolism), XMedGPT demonstrated robust generalizability, outperforming the top-performing GMAI model [80] by 16.7%.

Notably, the effectiveness of clinician-centric multimodal interpretability was evaluated across three key pillars. Specifically, XMedGPT demonstrated superior grounding performance, achieving an Intersection over Union (IoU) score of 0.703 across 141 anatomies and a Kendall’s tau-b correlation coefficient of 0.479 ( $P < 0.05$ ), indicating strong alignment between rationales and clinical outcomes. For uncertainty quantification, the model also achieved an AUC of 0.862 on visual question-answering (VQA) tasks and a 0.764 AUC on report generation. These results underscore the clinical viability of fusing trustworthy AI systems into routine clinical practice, elevating diagnostic precision while safeguarding against diagnostic cascades triggered by opaque AI errors. In summary, XMedGPT represents a significant leap forward in the integration of AI into healthcare, combining multi-modal data synthesis, interpretability, prognostic precision, and real-world validation to deliver a robust, clinician-ready decision-support tool with broad clinical applicability.

## Results

### XMedGPT Achieves Superior Performance Across 23 Benchmarks Beyond 38 Imaging Modalities

To rigorously benchmark XMedGPT against leading GMAI models, we conduct a comprehensive evaluation across five core tasks: single-label diagnosis, multi-label diagnosis, visual-question answering (VQA), multiple-choice reasoning, and image captioning. For single-label diagnosis, XMedGPT is tested on nine datasets spanning organ recognition (OrganAMNIST, OrganCMNIST, OrganSMNIST) [88] and lesion classification (PathMNIST, OCTMNIST, PneumoniaMNIST, BreastMNIST, PAD-UFES-20 [68], MURA [73]), while multi-label diagnosis assesses its performance on diverse conditions including spinal (VinDr-SpineXR [66]), thoracic (VinDr-CXR [65], VinDr-PCXR [72], VinDr-Mammo [67], ChestMNIST [88]), and ocular (RFMiD [70], BRSET [64]) disorders. The VQA evaluation covers radiology (VQA-Rad [50], SLAKE [55]) and pathology (PathVQA [30]) datasets, probing anatomical and tissue-level understanding. To stress-test generalization, we leverage two large-scale multiple-choice benchmarks: OmnimedVQA (42 datasets, 8 modalities) [33] and GMAI-MMbench (284 datasets, 38 modalities, 18 tasks) [90], which surpass the scope of prior GMAI assessments. Finally, image captioning is evaluated on structured CXR datasets (IU-Xray [17], MIMIC-CXR [41]). This unified evaluation across tasks, modalities, and granularities not only demonstrates XMedGPT’s versatility but also establishes its superiority over existing GMAI models in both depth and breadth of medical understanding. We employ Macro-F1 as the primary metric for both single-label and multi-label diagnosis tasks, ensuring balanced evaluation across all classes. For VQA, we follow community standards by using F1-score as our main metric, supplemented by closed-ended accuracy (Closed-Acc) and open-ended recall (Open-Recall) for comprehensive analysis (see Table 1). Multiple-choice tasks are evaluated using answer selection accuracy. In assessing image captioning quality, we utilize both linguistic metrics (ROUGE-L, BLEU, METEOR) for text fluency and CheXpert- F1 for clinical precision, providing a dual perspective on generated captions.

As shown in Figure 2, XMedGPT achieves a unified F1 score of 0.639 across all five tasks, surpassing the previous state-of-the-art (SOTA) of 0.529 by MedRegA [80] by a significant margin. Notably, this performance is achieved with only 8 billion parameters, far fewer than the 40B parameters of MedRegA and MedDr [29]. For single-label diagnosis (See Table 2 for detail), XMedGPT attains a Macro-F1 score of 0.821, outperforming MedRegA 0.479 by a large margin. On the challenging long-tailed multi-label diagnosis task (See Table 2 for detail), XMedGPT achieves a Macro-F1 score of 0.262 across seven datasets, vastly exceeding prior models (ranging from 0.028–0.126). In addition, XMedGPT sets new SOTA results on major VQA benchmarks: 0.891 F1 on SLAKE, 0.634 on PathVQA, and 0.628 on VQA-RAD, outperforming 40B-parameter models MedDr and MedRegA (See Table 1 for detail). For closed-ended questions, it achieves 90.95% Closed-Acc on SLAKE and 92.39% on PathVQA, exceeding prior best scores of 89.90% and 90.21%. On VQA-RAD, XMedGPT attains 80.48% Closed-Acc and 45.07% Open-Recall, surpassing generalist models without fine-tuning. While LLaVA-Med [51] achieve higher Open-Recall with task-specific fine-tuning, XMedGPT outperforms similarly non-fine-tuned models like MedDr by 20.35% in fair comparisons. We also evaluated XMedGPT on GMAI-MMbench and OmnimedVQA, covering diverse clinical tasks and modalities. On OmnimedVQA, our model achieved 82.44% accuracy across 42 datasets (8 modalities), surpassing MedDr’s 72.54%. XMedGPT set SOTA performance

on 6 of 8 modalities, with notable improvements on CT (+19.0%) and Dermoscopy (+12.9%) (See Table 5 for detail). On GMAI-MMbench (18 clinical tasks, 284 datasets, 38 modalities), XMedGPT outperformed prior models on 17 tasks, with improvements exceeding 50% on eight tasks, highlighting its broad medical competency (See Table 4 for detail). Finally, for image captioning, we evaluated text similarity using NLG metrics (BLEU [71], ROUGE-L [12], METEOR [6]) and clinical correctness via CheXpert-F1 [79]. XMedGPT achieved SOTA performance on IU-Xray and MIMIC-CXR, with CheXpert-F1 scores of 0.479 (MIMIC-CXR) and 0.569 (IU-Xray) demonstrated gains of 14.3% and 4.6%, underscoring its clinical accuracy (See Table 3 for detail).

In direct comparison with GPT-4o, XMedGPT establishes itself as the unequivocal leader across all five core medical tasks, outperforming both general-domain and specialized medical models. On single-label diagnosis, XMedGPT achieves a 0.791 F1-score, more than doubling GPT-4o’s performance (0.331) and significantly surpassing MedDr’s 0.281. For multi-label diagnosis, XMedGPT attains a 0.258 F1-score - nearly twice as high as GPT-4o’s 0.131, while previous medical SOTA models MedRegA and MedDr score below 0.100. In image captioning, XMedGPT demonstrates comprehensive superiority: it exceeds GPT-4o by 33.6% in METEOR (linguistic quality) and achieves a tenfold improvement in CheXpert-F1 (clinical accuracy). This advantage scales consistently - on the comprehensive GMAI-MMbench (284 datasets), XMedGPT outperforms GPT-4o by 29.1% overall, with particularly striking gains exceeding 50% on five critical clinical tasks. Together, these results underscore XMedGPT’s unique position as the first model to consistently surpass both leading general-purpose LLMs and specialized medical AI.

### **XMedGPT is a Prognostic-Capable MLLM with Superior Performance Over Task-Specific Models**

To evaluate the potential of using GMAI model in prognostic decision-making that integrating multiple data sources, we conducted three challenging prognostic tasks: Progression-Free Survival (PFS) prediction for lung cancer patients undergoing tyrosine kinase inhibitors (TKIs) treatment, overall survival (OS) prediction for patients with NSCLC tumors, and OS for patients with neuro-oncology (e.g., Glioma).

#### **Progression-Free Survival Prediction in TKI-Treated Lung Cancer**

XMedGPT demonstrated robust performance in predicting progression-free survival (PFS) for lung cancer patients treated with tyrosine kinase inhibitors (TKIs), significantly outperforming existing methods. PFS prediction, which evaluates the time from treatment initiation to disease progression or death, is critical for risk stratification and guiding personalized therapy. To address the complexity of integrating diverse clinical data—including lung CT scans, patient demographics, medical history, disease characteristics (e.g., mutations, smoking status, metastasis), and TKI treatment parameters—we developed a model trained on a multicenter dataset from two hospitals ZE (n=238), NF (n=85) and evaluate on two external dataset from another two hospitals JX (n=58), and HN (n=49). The model was optimized to predict whether patients would achieve PFS exceeding 14 months, a clinically significant threshold based on established guidelines linking prolonged PFS to favorable treatment response and survival outcomes in TKI therapy. Evaluation on the JX and HN cohorts demonstrated strong performance of our model, achieving an AUC of 0.725 (95% CI: 0.636–0.812), which represents a 16.7% improvement over the leading task-specific model [18] (AUC: 0.621, 95% CI: 0.511–0.729). This corresponds to a 25.7% increase in accuracy. Kaplan-Meier analysis further confirmed the model’s clinical utility, showing statistically significant risk stratification on both JX cohort (log-rank  $P < 0.001$ ) and HN cohort (log-rank  $P = 0.008$ ), whereas the task-specific model failed to achieve significance in JX cohort ( $P = 0.085$ ). Similarly, when compared to the leading general-purpose model, GPT-4o, our model attained higher accuracy (0.764, 95% CI: 0.682–0.841) and more robust risk stratification ( $P = 0.008$ ). In contrast, GPT-4o exhibited weaker discrimination ( $P = 0.029$ ) and lower accuracy (0.643, 95% CI: 0.551–0.729), highlighting the limitations of general-purpose MLLMs in clinical settings.

#### **Overall Survival Estimation for NSCLC Patients**

XMedGPT demonstrated robust predictive performance in estimating overall survival (OS) for non-small cell lung cancer (NSCLC) patients. OS, defined as the duration from diagnosis to death from any cause, is a critical endpoint for risk stratification and therapeutic decision-making. To address the heterogeneity of immunotherapy response, we incorporated baseline CT imaging features, TNM

staging, and histopathological subtypes into a unified predictive framework. The model was trained on the Lung1 dataset (n=420) and externally validated on the RADIO cohort (n=133), with optimization

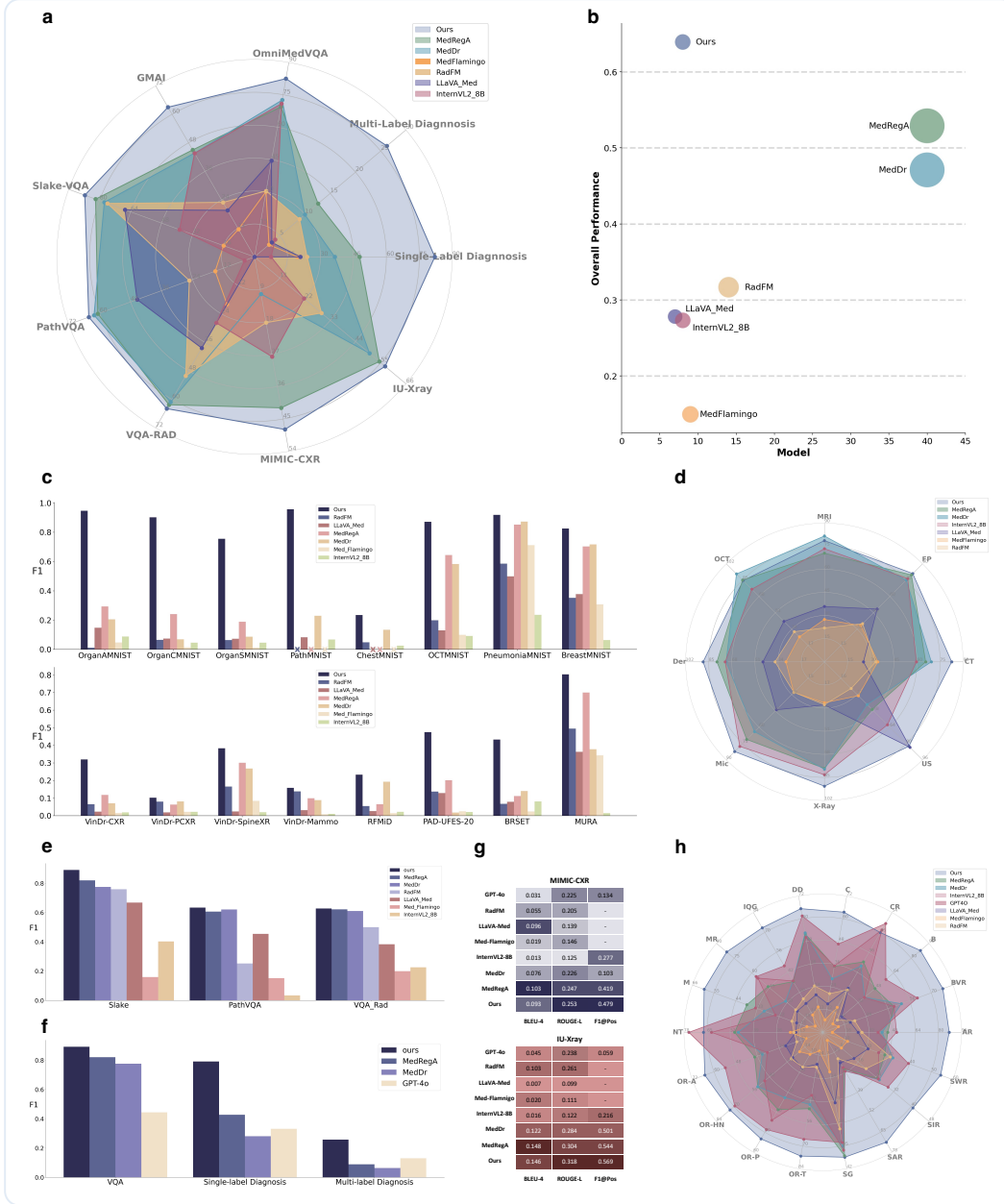


Figure 2: **a**, XMedGPT consistently outperforms other generalist biomedical models across five core tasks: single-label diagnosis, multi-label diagnosis, visual question answering (VQA), multiple-choice reasoning, and image captioning. **b**, Overall task performance relative to model scale. **c**, Performance on single- and multi-label diagnosis tasks, evaluated using F1-score and micro-F1-score, respectively. **d**, Accuracy on the OmniMedVQA multiple-choice benchmark, covering eight medical modalities from 42 datasets. **e**, Comparison of closed-ended accuracy, F1-score, and open-ended recall for medical VQA; 'x' indicates missing results in the original publications. **f**, Benchmarking against GPT-4o and other leading GMAI models on VQA, single-label, and multi-label diagnosis tasks. **g**, Image captioning performance on MIMIC-CXR and IU-Xray, assessed using BLEU, ROUGE-L, and CheXpert-F1 metrics. **h**, Accuracy on the GMAI-MMbench multiple-choice benchmark, covering 284 datasets, 38 modalities, and 18 clinical tasks.



targeting 2-year survival—a clinically relevant benchmark aligned with prior studies. On independent validation, XMedGPT achieved an AUC of 0.706 (95% CI: 0.604–0.803), representing a 18.1% improvement over the leading clinical risk score (AUC: 0.598, 95% CI: 0.486–0.703). Kaplan-Meier analysis revealed statistically significant stratification between risk groups ( $P < 0.001$ ). In contrast, the leading task-specific model’s clinical risk score failed to achieve significant discrimination ( $P = 0.125$ ). When evaluated against GPT-4o, XMedGPT exhibited superior accuracy (0.784; 95% CI: 0.714–0.850) compared to GPT-4o (0.699; 95% CI: 0.624–0.782), alongside stronger risk stratification ( $P < 0.001$  for XMedGPT versus  $P = 0.029$  for GPT-4o). These results highlight the limitations of general-purpose models in oncology applications and underscore the potential of using Medical LLMs in prognostic clinical decision-making.

### **Glioblastoma Survival Estimation for Extensive Neuro-Oncology with MRI Biomarkers**

Our study further establishes the prognostic capability of XMedGPT in predicting overall survival (OS) for glioblastoma (GBM) using preoperative MRI scans, demonstrating its scalability across distinct tumor types and imaging modalities compared to previous prognostic tasks in lung cancer (CT-based). This extension to neuro-oncology, with fundamentally different tumor behavior and imaging characteristics, highlights our model’s generalizability to diverse oncological domains. The model was trained on the UPENN-GBM cohort ( $n=585$ ) and validated on the BraTS dataset ( $n=163$ ), with optimization targeting one year OS - a critical benchmark set by previous works for clinical decision-making in neuro-oncology. In the BraTS validation cohort, XMedGPT achieved an AUC of 0.720 (95% CI: 0.634–0.800), outperforming the baseline model (AUC: 0.701, 95% CI: 0.614–0.781) by 2.7%. Kaplan-Meier analysis stratified patients into distinct prognostic groups ( $P < 0.001$ ). When compared to GPT-4o, XMedGPT exhibited superior accuracy (0.652; 95% CI: 0.577–0.730) relative to GPT-4o (0.509; 95% CI: 0.429–0.583) and more precise risk stratification ( $P < 0.001$  for XMedGPT versus  $P = 0.365$  for GPT-4o), underscoring the necessity of domain-specific adaptation in neuro-oncological AI.

### **XMedGPT is A Clinician-Centric AI Assistant for Multi-Modal Interpretation and Trustworthy Support**

XMedGPT bridges the gap between opaque AI systems and clinically actionable insights by unifying visual-textual evidence, structured reasoning, and reliable uncertainty quantification. This framework ensures clinicians can audit AI outputs efficiently, mitigating risks of misguidance from unverifiable predictions.

#### **Precise Uncertainty Quantification for Clinically Reliable AI Responses**

Motivated by the success of semantic entropy in detecting confabulations across various language models and domains [20], we aimed to evaluate its applicability in the medical domain, specifically in Visual Question Answering (VQA) tasks, and to enhance sentence-level uncertainty estimation in medical report captioning. We observed that both Semantic Entropy (SE) and its discrete approximation (Discrete SE) suffer from imprecise estimates when candidate answers are similar—an issue that becomes more pronounced when sampling is limited, as sampling in multimodal large language models (MLLMs) is computationally expensive due to their large parameters. This leads to overconfidence as entropy is underestimated. To address this, we reformulated the semantic entropy calculation to incorporate a more nuanced approach that accounts for response confidence, thereby significantly improving the reliability of uncertainty estimation.

We first evaluated our method across four distinct medical VQA datasets: SLAKE, VQA-RAD, PathVQA, and VQA-Med [7]. Our enhanced SE approach demonstrated clear improvements over both traditional SE and Discrete SE, with an average performance increase of 9.40% across all datasets. Notably, on the SLAKE dataset, the area under the curve (AUC) improved 14.1% from 0.71 to 0.81, and similar improvements were observed on the VQA-RAD dataset (improved 9.1% from 0.734 to 0.801). These results underscore the robustness and reliability of our method in uncertainty estimation, a critical aspect of high-stakes medical decision-making.

Having validated the effectiveness of our uncertainty estimation approach on medical VQA tasks, we extended it to the domain of medical report captioning for sentence-level uncertainty estimation, as illustrated in Figure 7. For each sentence generated in a medical report, our system generates multiple questions based on the sentence using a large language model. The consistency between the answers to these questions and the caption is assessed, with semantic entropy calculated to quantify

uncertainty for each sentence. We evaluated the reliability of the uncertainty estimates on a subset ( $n = 200$ ) of the MIMIC-CXR test dataset. As the number of questions increased from 1 to 5, the AUC improved from 0.676 to 0.764, reflecting a 13.02% enhancement. This substantial improvement

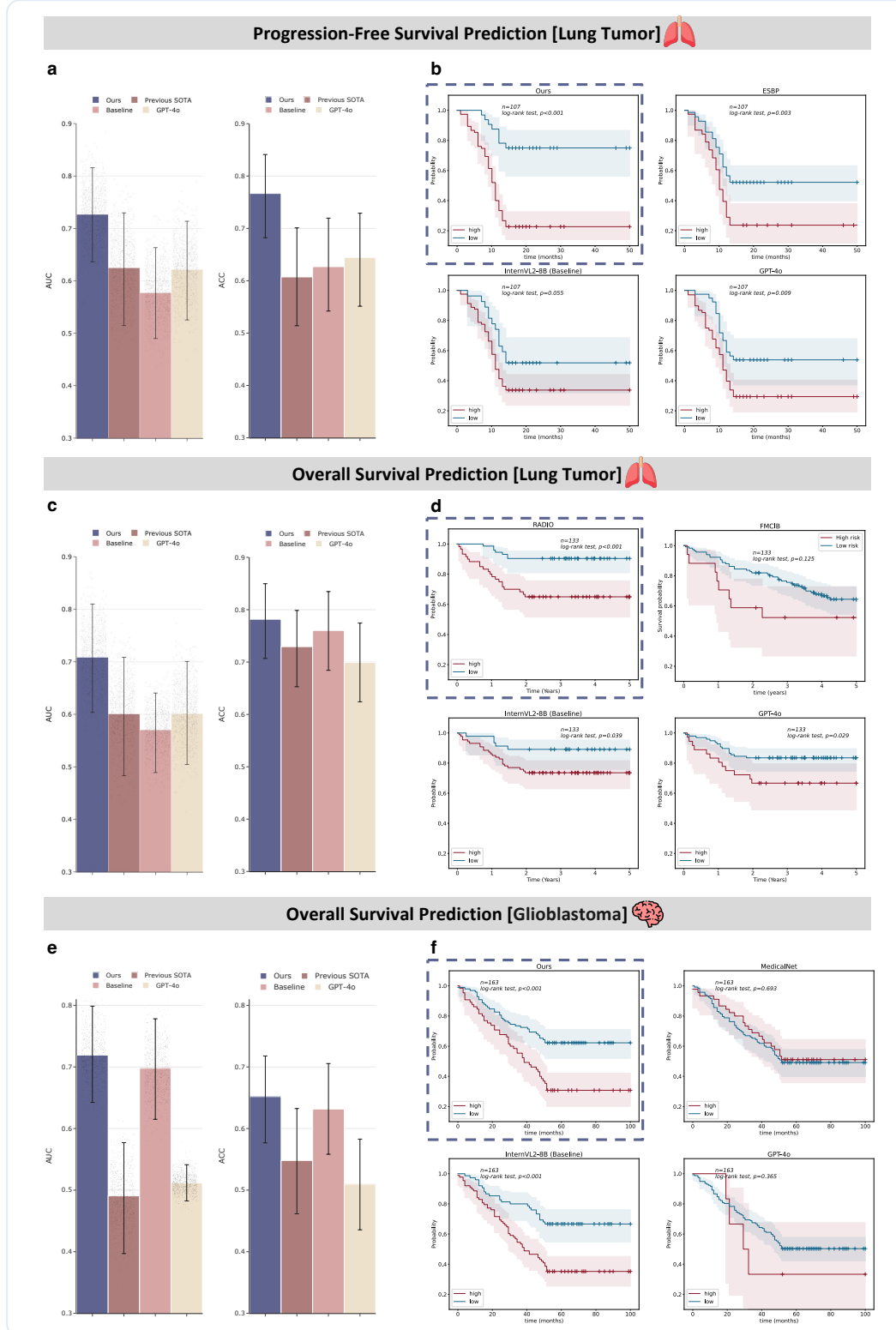


Figure 3: **a, c, e**, Performance comparison of foundation model-based approaches and baseline methods using AUC and F1 scores. Panel a shows results for 14-month progression-free survival prediction, c for 2-year overall survival prediction in non-small cell lung cancer (NSCLC), and e for 1-year overall survival prediction in glioblastoma. Refer to the Methods section for implementation details. **d,e,f**, Kaplan–Meier survival curves stratified by model-predicted risk groups across the three prognostic tasks. Risk thresholds were determined using internal validation sets to ensure fair comparison across methods.

demonstrates the effectiveness of combining semantic entropy with test-time scaling for estimating sentence-level uncertainty.

### Visual and Textual Interpretation for Clinically trusted AI Responses

Our clinical reasoning framework for medical report generation, designed to mirror diagnostic workflows, significantly enhances the interpretability and reliability of AI-generated reports. The five-step process—anatomical structure identification, region localization, region-specific description, holistic analysis, and final report synthesis—integrates patient history, chief complaints, and imaging findings to produce structured, evidence-backed outputs. By explicitly linking clinical context to visual evidence, the model achieves traceable anatomical localization, with region markings demonstrating 95.6% matchness to reference annotations and a mean Intersection over Union (IoU) of 66.6%. This visual grounding ensures that early reasoning steps provide spatially precise evidence, a critical advancement over prior methods.

Training on the MIMIC-CXR dataset involved supervised fine-tuning (SFT) with 10,000 samples for long chain-of-thought reasoning, followed by reinforcement learning via Direct Preference Optimization (DPO) on 8,201 high/low-scoring report pairs. Evaluation on a test set annotated with Chest-Imagenome-derived regions revealed a 6.05% average improvement across clinical metrics (CheXpert F1, Radgraph F1, CheXpert Similarity) compared to non-reasoning baselines. DPO further refined report quality, elevating CheXpert F1 from 0.362 to 0.372. The model’s reasoning coherence was quantitatively validated using Kendall’s tau-b correlation, which measured alignment between intermediate reasoning paths and final conclusions. Scores of 0.479 (consistency) and 0.474 (completeness; both  $P < 0.05$ ) indicate strong logical agreement.

### XMedGPT is A Medical-Omni Model Integrating Audio and Regional Functionality for Flexible Human-AI Interaction

XMedGPT is a groundbreaking Medical-Omni model that seamlessly integrates both audio and dual regional functionality, revolutionizing human-AI interaction and expanding its applicability across a broad spectrum of biomedical tasks. By incorporating audio capabilities, the model facilitates a more intuitive and natural communication channel between healthcare professionals and the AI system, streamlining clinical workflows. Meanwhile, the integration of regional inputs allows the model to perform advanced pixel-level analysis including region recognition and localization tasks. This dual functionality enables seamless interaction, where users can easily localize lesions and analyze specific regions of interest, providing a powerful tool for both healthcare providers and patients.

We rigorously evaluated regional performance of our model across diverse biomedical tasks, including region recognition, lesion localization, region-based visual question answering (VQA). We use 1,272 test samples for region recognition and 1,000 test samples for lesion detection test examples from a variety of segmentation and detection datasets to assess region recognition and lesion detection capabilities. For region recognition, the model was tasked with identifying 141 distinct regions, each provided with a corresponding bounding box. The F1-score was used as the metric to evaluate its recognition performance. In the lesion localization task, the model was required to accurately localize lesions based on their designated names. Intersection over Union (IoU) was used to assess the localization accuracy. For region VQA, we tested the model on the Med-GRIT dataset [34], which contains 30,000 question-answer pairs across eight different medical imaging modalities. The Med-GRIT dataset includes four sub-tasks: Referring Object Classification (ROC), Referring Captioning (RC), Visual Grounding (VG), and Medical Image Analysis (MIA). In line with the BiRD framework, we employed acc@0.5 to evaluate ROC, SPICE for RC, recall@0.5 for VG, and mBMR (average of BLEU-2, METEOR and ROUGE-L) for MIA, ensuring comprehensive evaluation across each task.

The overall performance across the three primary tasks is illustrated in Figure 5. While previous models, such as MedRegA [80] and BiRD [34], have introduced anatomical localization into MLLMs, their performance falls short when compared to our XMedGPT. For region recognition, XMedGPT achieved an F1-score of 0.774, surpassing SOTA approach MedRegA F1-score 0.359, lowering our method by 53.6% , demonstrating its superior ability to accurately identify and analyze regions. In anatomical localization, XMedGPT achieved an IoU of 0.703, outshining MedRegA 0.309 by a large margin, underscoring its precision in accurately pinpointing lesions (See Table 6 for detail). In the region VQA task, XMedGPT achieved an average score of 0.733 across four sub-tasks, outperforming the previous state-of-the-art model, BiRD, by 29.4%, with improvements ranging from 18.0% to 40.6% across the individual sub-tasks (See Table 7 for detail). These results highlight the advanced capabilities of XMedGPT in pixel-level analysis across diverse biomedical tasks. Beyond general performance, we also assessed the model’s ability to handle different anatomical structures. XMedGPT consistently outperformed MedRegA across all structures except for the skeleton, where it was slightly behind. For lesion localization, XMedGPT excelled in all anatomical structures, surpassing MedRegA across the board. In region VQA, the model again demonstrated superior performance, outperforming BiRD across all structures. Furthermore, when assessed across different modalities, XMedGPT maintained its superiority, outpacing BiRD in all modalities except for Endoscopy in the Referring Captioning (RC) task, where it performed slightly below BiRD (lower by 1%). Notably, in CT, X-ray, and Fundus imaging, XMedGPT led BiRD by margins ranging from 34.5% to 58.1% averaged on four tasks. These results underscore the robustness, adaptability, and generalizability of XMedGPT in pixel-level analysis and biomedical task performance.

Incorporating audio capabilities further amplifies the model’s versatility. We fine-tuned the model with a subset of the pre-trained dataset, converting text into audio using the Speechh5 model [4], which includes a diverse array of audio styles. Our model with audio input surpasses the baseline model for a large margin, achieving an average improvement of 0.399 (from 0.133 to 0.532) across all benchmarks compared to the baseline method (Intern-Omni) [10] (See Table 8 for detail). Although audio input slightly lagged behind text input across most benchmarks, it performed equally well in more complex multi-label diagnostic tasks, only lowering by 0.044 (from 0.250 to 0.206) averaged on four multi-label diagnosis tasks (VinDr-CXR, VinDr-PCXR, VinDr-SpineXR, VinDr-Mammo), demonstrating the reliability and robustness of audio input. These results highlight the potential of combining audio and regional inputs to offer a more flexible, robust, and interactive model for medical applications, enhancing the model’s overall utility in human-AI collaboration.

### **XMedGPT Unleashing Robust Generalizability Across Diverse Tasks and Ensuring Reliable AI with Guardrail Capabilities**

The external validation on in-house data with different distribution with the training data on diverse tasks the efficient application of a single, pre-trained model to a wide array of tasks, without the need for extensive retraining or data annotation for each new distribution. XMedGPT, pre-trained on a large-scale medical dataset incorporates over 114 open-source datasets, exhibits exceptional generalizability across various tasks without the need for further fine-tuning. We evaluated XMedGPT’s generalizability on in-house data collected from Sun Yat-sen Memorial Hospital, Sun Yat-sen University, which contains well-annotated masks for 11 clinically significant diseases. We assessed its performance on four primary tasks: Multiple-Choice, Diagnosis, Localization, and Visual Question Answering (VQA). For Multiple-Choice tasks, we use accuracy to evaluate performance. For Diagnosis, we use the F1 score, and for Localization, we assess performance using IoU. In VQA, we employ the LLM-as-Judge approach, evaluating the generated answers across three aspects: accuracy, consistency, and clinical relevance as the NLG metric alone does not fully capture semantic similarity with the reference.

For Multiple-Choice tasks, XMedGPT achieved an accuracy of 94.0%, outperforming MedRegA’s 80.6% by 16.6%. Notably, the baseline model InternVL2-8B showed significantly better performance compared to large-scale medical models such as LLaVA-Med, RadFM, Medflamingo, and MedDr, indicating that existing medical MLLMs struggle with generalizing to new distributions, even in simpler tasks like multiple-choice. In the Diagnosis and Localization tasks, XMedGPT also performed exceptionally, achieving an F1 score of 0.768 and an IoU of 0.431, surpassing MedRegA’s 0.189 and 0.221 by a remarkable margin. For VQA task (See Table 10 for detail), XMedGPT achieved average scores of 8.61 across three evaluation aspects, outperforming previous SOTA MedDr by 7.9%. Notably, when evaluating accuracy, consistency, and clinical relevance—the key metrics for assessing



the correctness of generated answers—XMedGPT demonstrated a marked advantage, improving 7.2%, 6.9%, and 8.6% compared to previous SOTA, indicating its reliability and robustness in VQA tasks.

We further assessed XMedGPT’s performance in Region Recognition and Lesion Localization across 11 clinically significant diseases, using both internal and external validation datasets (See Table 9 for detail). In Region Recognition, XMedGPT’s performance on the external dataset was slightly lower by 0.12 on average compared to the internal dataset. The model’s performance was less robust in kidney and prostatic cancers. However, in certain diseases, such as cerebral hemorrhage and pancreatic cancer, the model outperformed the internal dataset, showcasing its strong generalizability. Similarly, for Lesion Localization, XMedGPT showed a slight decrease of 0.19 on the external dataset, but excelled in diseases like cerebral hemorrhage and pancreatic cancer, surpassing internal dataset results. Notably, in the challenging task of detecting Pulmonary Embolism, XMedGPT showed a drop of 0.44 on the external dataset. For liver cancer, the model achieved an improvement of 9.2% in IoU for lesion localization. These results highlight the robust generalizability of XMedGPT across diverse clinical tasks and diseases, demonstrating its ability to maintain reliable and consistent performance on unseen data. This ensures its applicability in real-world clinical settings, making it a highly effective and adaptable tool for medical applications.

In addition to its remarkable generalizability, we also assessed the guardrail capabilities of XMedGPT—an essential feature that ensures the model’s reliability and safety in clinical environments. Guardrails are vital for preventing the model from making incorrect or unsafe predictions, particularly in biomedical tasks. For instance, when given image-specific instructions such as “Detect the right kidney from the image,” if no kidney is present, the model is expected to respond appropriately, saying, “Sorry, I cannot find the right kidney in the image.” We refer to such cases as “mismatch scenarios”. XMedGPT demonstrated exceptional guardrail performance, successfully detecting 83.02% of mismatch scenarios, while previous models failed to identify any. This impressive result underscores the model’s capacity to detect potential mismatches and ensure reliable, safe predictions, highlighting its suitability for real-world clinical applications.

## Discussion

In this study, we present XMedGPT, a new Medical Multimodal Large Language model expanding the capabilities of Generalist Medical AI (GMAI) to previously underexplored yet clinically significant decision-making tasks and enabling seamless collaboration with flexible interaction modes and trustworthy responses. Through extensive evaluation on 38 benchmarks covering 18 medical modalities, we show that XMedGPT achieves superior performance over existing GMAI models, without requiring any further fine-tuning. While previous GMAI models have focused on relatively simple biomedical tasks, such as image classification, visual question answering and captioning, with intended applications for diagnosis and lesion detection, XMedGPT firstly extends the capabilities of GMAI to more complex clinical decision-making tasks by using its ability to synthesize information from multimodal data sources, such as radiography, patient demographics and medical history. The superior performance on progression-free survival prediction and overall survival prediction tasks demonstrated that the multimodal fusion capabilities of XMedGPT can be effectively leveraged to improve the clinical decision-making process. In addition, we conducted sufficient external validation across diverse modalities, diseases, and tasks to evaluate the generalizability and robustness of XMedGPT considering the heterogeneity of data distribution across different sources. The results show that XMedGPT can generalize well to unseen data and tasks, demonstrating its potential for real-world clinical applications. However, we observed that the external validation performance on detecting Pulmonary Embolism showed a significant performance drop compared to the internal validation results. This observation suggests that the adaptation to small target detection is still a challenging task for GMAI models and requires further investigation to attain comprehensive generalizability for GMAI models. Importantly, XMedGPT holds presents impressive guardrail capabilities for preventing the model from making incorrect or unsafe predictions, ensuring the model’s reliability and safety in clinical environments.

To foster practical clinical applications with human-AI collaboration, a major challenge is to equip the model with flexible interaction modes and interpretable, actionable and easily verifiable responses. Our XMedGPT introduce a mechanism that combines the model’s responses with sentence-level uncertainty, detailed diagnostic reasoning, and grounding evidence, providing an effective solution for

the model to communicate with human experts in a more interpretable and trustworthy manner. We observed the reliability of estimated uncertainty improved with the scaling of the sampled question-answer pairs, which suggests that the test-time scaling of the model can be an effective strategy to harness the model’s uncertainty estimation capabilities. Furthermore, we demonstrated that the response associated with detailed diagnostic reasoning and grounding evidence not only provides a more interpretable and actionable response but also improve the performance on the challenging captioning tasks. In addition, fine-tuning on large-scale image-level and pixel-level annotations and further training on audio data provided the model with the ability to support a variety of input-output formats such as images, text, audio, and region-based inputs—offering enhanced adaptability and interaction. The evaluation on diverse regional-related tasks showed that XMedGPT can effectively handle region-based inputs and detect more than 200 regions across all anatomical structures. Our model with audio input also attained much superior performance than baseline model and achieved competitive performance with text input. Both of the results suggest that XMedGPT demonstrate its potential for providing flexible interaction modes for human-AI collaboration.

Despite promising results in clinical decision-making tasks, such as progression-free survival (PFS) and overall survival (OS) prediction, the model’s performance was evaluated on relatively small cohorts—49 and 58 patients for PFS from two centers, 133 patients for lung cancer overall survival prediction from one center, and 163 patients for glioma tumor overall survival prediction from one center. Thus, further validation in larger, multi-center cohorts is necessary before clinical implementation, particularly for high-stakes applications, which will require regulatory approval through prospective trials involving diverse patient populations. Additionally, while the model performed well on a variety of external validation tasks, it showed a significant drop in performance for small target detection tasks, such as pulmonary embolism and kidney and prostate cancer recognition. This highlights the challenge of adapting generalist medical AI to small target detection, and future research should address issues related to data diversity, resolution, and detection algorithms. Moreover, the model currently lacks the capability to process video inputs or 3D medical images, which are common in medical imaging. Expanding the model to handle these formats requires collecting and annotating large-scale video and 3D datasets, and future work should focus on developing strategies to generate and leverage such datasets to enhance the model’s ability to process 3D medical images.

## Conclusion

XMedGPT introduces a clinician-centric paradigm for Generalist Medical AI (GMAI) that addresses critical limitations in multi-modal explainability, prognostic accuracy, and human-AI collaboration. By combining visual lesion localization with text-based diagnostic reasoning, alongside a novel Reliability Indexing mechanism that quantifies prediction uncertainty, XMedGPT significantly reduces AI-induced errors by 15.2%, allowing clinicians to confidently validate high-stakes outputs. Trained on a diverse dataset of 7 million multi-modal medical data points, XMedGPT excels in detecting subtle longitudinal tumor changes and synthesizing multi-visit data for prognostic decision-making. It achieves a 26.9% average improvement in AUC over previous leading models for overall survival and progression-free survival prediction, encompassing both high-incidence cancers (e.g., lung adenocarcinoma) and high-mortality diseases (e.g., glioblastoma). Its robust generalizability across 141 anatomical regions and 40 modalities, validated through extensive external trials, positions XMedGPT as the first GMAI with scalable, clinician-ready utility. This system not only advances precision oncology but also establishes a new benchmark for AI tools that enhance diagnostic autonomy while preserving clinical expertise, driving the integration of trustworthy AI into real-world care pathways.

## Methodology

### Dataset Curation for Pretraining

For the pretraining of the Generalists Medical AI XMedGPT, we utilized a diverse collection of publicly available medical datasets to create a comprehensive, large-scale dataset tailored for image-level tasks, region-level tasks, and clinical applications. The image-level dataset comprises 5,468,115 pairs of images and corresponding questions. This dataset is designed to support tasks such as medical diagnosis, visual question answering, and image captioning. The pixel-level dataset includes 1,686,677 pairs of images and questions, each annotated with regional information. This pixel-level

dataset encompasses 141 distinct regions of interest. The inclusion of these medical tokens allows the model to process a wide range of biomedical instructions and interpret long-context information, thereby enhancing its capacity for nuanced understanding across different medical contexts.

To support the pretraining of XMedGPT across various medical tasks, we developed a set of tailored prompts designed for different medical applications. Previous research has shown that diverse prompts during pretraining can significantly improve the model’s ability to follow instructions and enhance its performance on downstream tasks. The prompts for each task are illustrated in Figure 10 and Figure 11. For each task, we begin by providing a template and then specify the task-specific instructions. To further diversify the prompt styles, we employ large language models (e.g., GPT-4) to generate a wide range of variations in the task instructions. For example, for the lesion detection task, we start with the template: “Can you analyze this <modality> image and identify the <class> present?”, where <modality> represents the imaging modality (e.g., X-ray, MRI) and <class> denotes the type of lesion (e.g., tumor, fracture). We then use GPT-4 to generate diverse additional, varied instructions, such as: “In this <modality> image, could you detect all instances of <class>?” and “Please locate and identify all visible <class> in the <modality> scan.” These instructions provide different ways of asking the same task, ensuring that the model is exposed to a wide range of phrasing and perspectives. By incorporating this diversity of prompts, we aim to improve the model’s ability to understand and follow task-specific instructions, thereby making it a versatile and user-friendly tool for a broad spectrum of medical applications.

### Model design and pretraining

The training of XMedGPT is conducted using a multi-modal transformer architecture that combines vision and language modalities. The model architecture is based on InternVL-2, a state-of-the-art multi-modal transformer model that has been pre-trained on a large-scale dataset of image-text pairs. As demonstrated in previous studies, supervised fine-tuning on pre-trained models for domain-specific applications achieves superior performance compared to training from scratch. To adapt the model to the medical domain, we fine-tune the InternVL-2 model on our large-scale medical dataset using a supervised learning approach for one epoch.

### Benchmark datasets

We evaluated XMedGPT across 23 benchmarks, spanning a wide range of medical tasks including single-label diagnosis, multi-label diagnosis, multiple-choice questions, visual question answering (VQA), and image captioning. These benchmarks were based on various publicly available biomedical datasets. For single-label diagnosis, we used nine datasets, covering 34,821 samples for organ recognition (OrganAMNIST (n=17,778), OrganCMNIST (n=8,216), OrganSMNIST (n=8,827)) and 13,193 samples for lesion recognition (PathMNIST (n=7,179), OCTMNIST (n=999), PneumoniaMNIST (n=623), BreastMNIST (n=155), PAD-UFES-20 (n=1,044), MURA (n=3,193)). These datasets focus on identifying specific organs or lesions from medical images, testing the model’s capacity to perform classification tasks. In multi-label diagnosis, we assessed the model’s performance on six lesion classification datasets. These included 2,077 samples for spinal lesions (VinDr-SpineXR), 8,387 samples for thoracic diseases (VinDr-CXR (n=3,000), VinDr-PCXR (n=1,387), VinDr-Mammo (n=4,000)), and 3,894 samples for ocular lesions (RFMiD (n=640), BRSE (n=3,254)). Multi-label classification tasks require the model to identify multiple lesions within a single image, providing a more complex challenge for lesion recognition. The visual question answering benchmarks included two commonly used radiology datasets, which together cover 1,512 samples across five anatomical regions (VQA-Rad (n=451), SLAKE (n=1,061)), and an additional 6,761 samples from a pathology dataset (PathVQA), which combines anatomical and tissue-specific details. These tasks test the model’s ability to understand and respond to medical questions about images, ranging from simple anatomical recognition to more complex tissue-specific inquiries. To further evaluate the model’s generalizability across clinical tasks and modalities, we also tested it on two comprehensive multiple-choice benchmarks: OmnimedVQA and GMAI-MMbench. OmnimedVQA includes 72,683 samples sourced from 42 datasets, representing 8 modalities, while GMAI-MMbench encompasses 21,281 samples derived from 284 datasets. The latter covers a broad spectrum of 38 medical image modalities, 18 clinical tasks, 18 medical departments, and 4 levels of perceptual granularity. For image captioning, we evaluated XMedGPT on two widely used chest X-ray (CXR) datasets: IU-Xray (n=1,180) and Medical Information Mart for Intensive Care III-CXR (MIMIC-CXR) (n=4,710).

These datasets test the model’s ability to generate descriptive captions for medical images, a key task in enhancing automated medical reporting.

### **Implementation for prognostic decision making**

**Progression-free survival prediction for non-small cell lung cancer.** For this task, we utilized multi-center datasets collected from four institutions: the Second Affiliated Hospital of Zhejiang University School of Medicine (ZJ, n=238), the Affiliated Hospital of Jiaxing University (JX, n=58), Southern Medical University (NF, n=85), and Hunan Cancer Hospital (HN, n=49). The ZJ and NF cohorts were combined as the primary dataset, with an 80%:20% split for training and internal validation. The JX and HN cohorts were used exclusively for external validation. Each patient’s data comprised baseline lung CT scans (prior to treatment), smoking history, TNM stage, metastatic status, mutation status, and details of tyrosine kinase inhibitor (TKI) treatment. For some patients, longitudinal follow-up data were available, including additional lung CT scans taken at 1 month and 3 months in treatment. Progression-free survival (PFS) was defined as the duration from the date of initial drug administration to the time of either disease progression or death, whichever occurred first. PFS served as the primary outcome measure for assessing additional survival benefit, with the prognostic performance of ESPS [18] evaluated accordingly. Patients who remained alive without recorded progression were censored at the date of their last follow-up. Based on follow-up assessments, the median PFS for patients receiving EGFR-TKI treatment was determined to be 14 months. Patients were categorized into low-risk (good responders, PFS longer than median) and high-risk groups (poor responders, PFS shorter than median). Patients in the low-risk group were considered to have gained additional survival benefit, whereas those in the high-risk group were not considered to have gained additional survival benefit from EGFR-TKI therapy. For implementation details, our proposed method and baseline methods (InternVL2-8B and GPT-4o) leveraged these multi-visit CT scans, when available, to longitudinally assess disease progression. For the ESPS model specifically, we adhered to its standard protocol, initially cropping tumor regions from CT images before performing continuous fine-tuning on the ZJ and NF training datasets.

**Overall survival prediction for non-small cell lung cancer.** To evaluate overall survival (OS) in patients with non-small cell lung cancer (NSCLC), we utilized two publicly available datasets: LUNG1 and RADIO. The LUNG1 dataset comprises 422 patients with stage I–IIIB NSCLC who underwent radiation therapy at MAASTRO Clinic (Maastricht, the Netherlands). For this study, we selected 420 patients with annotated gross tumor volumes and survival data right-censored at 2 years. The selected cohort was used exclusively for tuning the models. The RADIO dataset includes 211 NSCLC patients (stage I–IV) referred for surgical treatment between 2008 and 2012. Following the convention of FMCIB, a subset of 144 patients includes tumor segmentations reviewed by two thoracic radiologists, and molecular profiling data (e.g., EGFR, KRAS, ALK mutations, gene expression arrays, RNA sequencing) are available for a majority of the cohort. Finally, we used a subset of 133 patients with annotated tumor volumes and survival data (right-censored at 2 years) as an independent test set. To assess prognostic performance, we classified patients into two risk categories based on their overall survival duration: those who survived beyond two years were designated as low-risk, while those who survived less than two years were considered high-risk. For model implementation, our proposed method and two baseline methods (InternVL2-8B and GPT-4o) utilized patient-level CT slices containing tumor regions as input, combined with textual clinical information. The models estimated the probability of a patient surviving longer than two years by averaging the predictions across all CT slices. For FMCIB, we followed the original implementation by extracting features from the foundation model and training a linear classifier using the LUNG1 cohort.

**Overall survival prediction for glioblastoma.** To assess overall survival in patients diagnosed with glioblastoma, we employed two publicly available datasets: UPEEN-GBM (n=585) and TCGA-GBM/BraTS (n=163). The UPEEN-GBM dataset was used for training and internal validation, following an 80%:20% split. The TCGA-GBM/BraTS cohort served as an independent external validation set. One-year overall survival (OS) was selected as the primary endpoint for all analyses. Both datasets provide four standard MRI modalities per patient: T1-weighted (T1), T1-weighted post-contrast (T1CE), T2-weighted (T2), and fluid-attenuated inversion recovery (FLAIR) images. For consistency and fair comparison across methods, we selected FLAIR as the primary imaging modality for training and evaluation. The model implementation followed the same framework as the NSCLC OS prediction task. Specifically, our approach and baseline methods (InternVL2-8B and



GPT-4o) processed the FLAIR slices containing tumor regions, supplemented with available clinical features, to predict whether a patient’s survival exceeded one year. Slice-level predictions were aggregated to produce patient-level survival probabilities. Additionally, we employed MedicalNet as a task-specific model; this foundation model was pre-trained on a diverse set of medical imaging modalities and tasks, providing strong generalizability for downstream survival prediction.

### Formulation for robust uncertainty estimation

**Formulation of Semantic Entropy.** The estimation for semantic entropy comprises three steps: (1) Sampling output sequences of tokens from the predictive distribution of the model given the input image  $\mathbf{x}$  and query  $\mathbf{q}$ . (2) Clustering generated sequences by their semantic similarity to obtain the cluster assignments for each sample. (3) Estimating semantic entropy by summing probabilities of the sequences in the same cluster. Specifically, given the input image  $\mathbf{x}$  and query  $\mathbf{q}$  as input to XMedGPT, we sample  $M$  output sequences of tokens,  $\{s^{(1)}, s^{(2)}, \dots, s^{(M)}\}$ , and their corresponding token probabilities,  $\{P(s^{(1)}|\mathbf{x}, \mathbf{q})\}, P(s^{(2)}|\mathbf{x}, \mathbf{q}), \dots, P(s^{(M)}|\mathbf{x}, \mathbf{q})\}$ . We sample all generations from XMedGPT with a temperature of 1.0 and a top-p sampling of 0.9. Next, we cluster the generated sequences into  $C$  groups that share the same semantic meaning. A semantic equivalence function  $E(\cdot, \cdot)$  is used to determine the semantic equivalence (entailment) between two sequences as follows:

$$E(s^{(i)}, s^{(j)}) = \begin{cases} 1, & \text{if } s^{(i)} \text{ and } s^{(j)} \text{ are semantically equivalent,} \\ 0, & \text{otherwise.} \end{cases} \quad (1)$$

By calculating the semantic equivalence between all pairs of sequences, we can distribute the samples into  $C$  clusters. Each semantic equivalence class  $c \in C$  contains sequences that are semantically equivalent, such that for any two sequences  $s$  and  $s'$  in the same cluster  $c$ , the equivalence  $E(s, s') = 1$  holds. The semantic equivalence function leveraged the idea of bidirectional entailment mentioned in [20]. That is, a sequence  $s$  is considered semantically equivalent to another sequence  $s'$  if and only if  $s$  entails  $s'$  and vice versa. In this study, we used the pre-trained DeBERTa-Large-MNLI model to calculate the entailment between two sequences. Having determined the semantic clusters  $C$ , we calculate the likelihood that a sequence generated by XMedGPT belongs to each cluster by computing the sum of the probabilities of the sequences as follows:

$$P(c|\mathbf{x}, \mathbf{q}) = \sum_{s \in c} P(s|\mathbf{x}, \mathbf{q}) = \sum_{s \in c} \prod_{t=1}^T P(s_t|\mathbf{x}, \mathbf{q}, s_{1:t-1}), \quad (2)$$

where  $P(c|\mathbf{x}, \mathbf{q})$  is the probability of cluster  $c$  given the input image  $\mathbf{x}$  and query  $\mathbf{q}$ , and  $P(s|\mathbf{x}, \mathbf{q})$  is the probability of sequence  $s$  given the input image  $\mathbf{x}$  and query  $\mathbf{q}$ . The semantic entropy  $H$  is then calculated as:

$$H = - \sum_c P(c|\mathbf{x}, \mathbf{q}) \log P(c|\mathbf{x}, \mathbf{q}), \quad (3)$$

where  $P(c|\mathbf{x}, \mathbf{q})$  is the probability of cluster  $c$ . The semantic entropy  $H$  is estimated by using the Rao-Blackwellized Monte Carlo integration over the clusters as follows:

$$H = - \sum_{i=1}^{|C|} P(C_i|\mathbf{x}, \mathbf{q}) \log P(C_i|\mathbf{x}, \mathbf{q}), \quad (4)$$

where  $P(C_i|\mathbf{x}, \mathbf{q}) = \frac{P(C_i|\mathbf{x}, \mathbf{q})}{\sum_{j=1}^{|C|} P(C_j|\mathbf{x}, \mathbf{q})}$  and  $\sum_{i=1}^{|C|} P(C_i|\mathbf{x}, \mathbf{q}) = 1$ . However, when all samples

belong to the same group or class, the benefit of Rao-Blackwellization diminishes because the method relies on the idea of conditioning on sufficient statistics (or sufficient information) to reduce variance in the estimate, i.e.,  $P(C_i|\mathbf{x}, \mathbf{q}) = 1$  for some  $i$ . In this case, the semantic entropy is highly biased and underestimates the true uncertainty without using the likelihood of the generated sequences. To address this issue, we propose a novel method to estimate the semantic entropy by considering the likelihood of the generated sequences when all samples belong to the same cluster. We first considering the entropy in each cluster as follows:

$$H_c = -P(c|\mathbf{x}, \mathbf{q}) \log P(c|\mathbf{x}, \mathbf{q}) = - \sum_{s \in c} \frac{P(s|\mathbf{x}, \mathbf{q})}{\sum_{s' \in c} P(s'|\mathbf{x}, \mathbf{q})} \cdot \log \left( \frac{P(s|\mathbf{x}, \mathbf{q})}{\sum_{s' \in c} P(s'|\mathbf{x}, \mathbf{q})} \right) \quad (5)$$

The semantic entropy is then calculated as:

$$H = \sum_{i=1}^{|C|} P(C_i|\mathbf{x}, \mathbf{q}) H_{C_i}. \quad (6)$$

This formulation ensures that the semantic entropy is accurately estimated when the sampling times  $M$  is small or when all samples belong to the same cluster, providing a more robust measurement of uncertainty in the model’s predictions. To verify the potential limitations of the Rao-Blackwellized Monte Carlo integration used in the original formulation, we conducted ablation studies on the four VQA benchmarks with sampling times  $M = 5, 10, 15, 20, 30$ . The results showed that when the sampling times  $M$  is small, the Rao-Blackwellized Monte Carlo integration underestimates the semantic entropy, leading to lower AUC scores. As the sampling times  $M$  increases, the AUC scores improve, and perform on par with the proposed method. However, the proposed method consistently outperforms the Rao-Blackwellized Monte Carlo integration across all sampling times, demonstrating its robustness and effectiveness in estimating semantic entropy. In addition, we extracted the  $(\mathbf{x}, \mathbf{q})$  pairs from the VQA benchmarks that have one cluster and compared the semantic entropy estimated by the Rao-Blackwellized Monte Carlo integration and the proposed method. The results showed that the proposed method achieved a higher AUC score than the Rao-Blackwellized Monte Carlo integration, indicating that the proposed method is more accurate in estimating the semantic entropy when all samples belong to the same cluster. These results demonstrate the effectiveness of the proposed method in estimating semantic entropy, particularly when the samples are highly clustered or when the sampling times are limited. The results showed that the proposed method estimated more accurate semantic entropy than the Rao-Blackwellized Monte Carlo integration, particularly when the samples are highly clustered.

**Sentence-level uncertainty estimation for medical report generation.** We extend this methodology to sentence-level uncertainty estimation in medical report generation. Robust and accurate uncertainty estimation in this context is essential for ensuring the reliability of generated reports and facilitating human-AI collaboration. In contrast to short-length generation tasks such as Visual Question Answering (VQA), medical report generation task, which involve the generation of longer sequences, are more prone to producing misleading or incorrect information. This is due to the text-biased nature inherent in modern large language models (MLLMs). An effective method for estimating the uncertainty in the generated reports is to combine the model’s capabilities in both captioning and VQA. As we have previously demonstrated the ability to estimate uncertainty in VQA tasks, we can apply the same approach to estimate the uncertainty of each sentence in the generated medical report by transforming it into a VQA task.

Given a generated report  $R = \{r_1, r_2, \dots, r_n\}$ , where  $r_i$  denotes the  $i$ -th generated sentence and  $n$  is the total number of sentences, we estimate the uncertainty of each sentence by generating  $M$  VQA pairs for each sentence  $r_i$ . These VQA pairs are related to the factual content of the sentence and are represented as  $(\mathbf{x}, \mathbf{q}_1, \mathbf{a}_1), (\mathbf{x}, \mathbf{q}_2, \mathbf{a}_2), \dots, (\mathbf{x}, \mathbf{q}_M, \mathbf{a}_M)$ , where  $\mathbf{x}$  is the input image,  $\mathbf{q}_j$  is the  $j$ -th question, and  $\mathbf{a}_j$  is the corresponding answer. To simplify the process, we formulate the questions and answers in a binary (yes/no) format. This binary structure enables more straightforward comparison of generated answers with reference answers. For instance, for the sentence "The patient has a mass in the right lung," the corresponding VQA question might be "Is there a mass in the right lung?" with the answer "Yes." For each sentence, with  $M$  VQA pairs, the model generates  $M$  output sequences of tokens:  $\{s^{(1)}, s^{(2)}, \dots, s^{(M)}\}$ , along with their associated token probabilities:  $\{P(s^{(1)}|\mathbf{x}, \mathbf{q}_1), P(s^{(2)}|\mathbf{x}, \mathbf{q}_2), \dots, P(s^{(M)}|\mathbf{x}, \mathbf{q}_M)\}$ . Since the binary structure of the questions and answers, the entailment between the generated answer and the reference answer can be easily calculated by using rule-based methods and clustering into two groups  $C_0$  and  $C_1$ , where  $C_0$  denotes the group of non-semantically equivalent answers and  $C_1$  denotes the group of equivalent answers. The semantic entropy  $H$  is then calculated as:

$$H = P(C_0|\mathbf{x}, \mathbf{q}) H_{C_0} + P(C_1|\mathbf{x}, \mathbf{q}) H_{C_1}, \quad (7)$$

where  $H_{C_0}$  and  $H_{C_1}$  are calculated by equation Equation (5). The sentence-level uncertainty estimation method is designed to provide a more accurate and robust measure of uncertainty in the generated medical reports, and thus provide a more verifiable and reliable tool for medical professionals to check and validate the generated reports.

## Formulation for medical reasoning

**Reasoning dataset curation.** We developed a step-by-step process for medical report generation, based on common clinical workflows: (1) Identify the anatomical structure to be examined, (2) Detect the regions of the anatomical structures, (3) Describe each detected region in detail, (4) Conduct a comprehensive analysis of all information, and (5) Summarize and generate the final report. To create a medical reasoning dataset, we used the Chest-ImageNome dataset, which includes aligned sentences and region-of-interest (ROI) annotations. The first step in our process was to divide the medical reports into individual sentences and extract the corresponding ROI annotations. Next, we rephrased the patient’s chief complaint and prior report, replacing abbreviations with their full forms and removing irrelevant information such as dates. For example, "Eval post-BAL" was replaced with "Evaluate after post-bronchoalveolar lavage." Using the aligned sentences, ROI annotations, patient chief complaint, prior report, and reference report, we employed GPT-4o to generate the reasoning process, moving from the findings section to the impression section. The detailed prompt is presented in Figure 12. The reasoning process integrates the patient’s previous conditions, current findings, and professional knowledge. To ensure the accuracy and reliability of the generated reasoning, a team of experienced radiologists reviewed and validated the output. Finally, we curated a dataset containing 10,562 samples for medical reasoning, each comprising comprehensive patient information and a detailed professional reasoning process.

**Training protocol for medical reasoning.** We first fine-tuned XMedGPT on the medical reasoning dataset using supervised fine-tuning for 1 epoch. This process fosters the model’s capability to generate comprehensive and accurate medical reasoning. To further enhance the reasoning ability of XMedGPT, we employed Direct Policy Optimization (DPO) for reinforcement learning. Following the process of DPO, we first curated 8,201 preference pairs  $(x, s_w, s_l)$ , where  $x$  is the inputs,  $s_w$  is the generated reasoning output with higher preference and  $s_l$  is the generated reasoning output with lower preference. Specifically, given the input  $x$  including the patient’s chief complaint, prior report, and chest x-ray image, we sampled  $K$  output sequences of tokens,  $\{s^{(1)}, s^{(2)}, \dots, s^{(K)}\}$ . For each output, we extracted the generated report in “Step 5” to calculate the preference score. The preference score is calculated as the CheXpert F1 score between the generated report and the reference report. The preference score is then used to determine the higher preference output  $s_w$  and the lower preference output  $s_l$ . Using the preference data and based on the Bradley-Terry model, the original objective for prior Reinforcement Learning from Human Feedback (RLHF)

$$\mathcal{L}_{\text{RLHF}} = -\mathbb{E}_{x \sim \mathcal{D}, s \sim \pi_\theta(s|x)} [r_\phi(x, s) - \beta \mathbb{D}_{\text{KL}} [\pi_\theta(s|x) \parallel \pi_{\text{ref}}(s|x)]] \quad (8)$$

is modified to

$$\mathcal{L}_{\text{DPO}}(\pi_\theta; \pi_{\text{ref}}) = -\mathbb{E}_{(x, s_w, s_l) \sim \mathcal{D}} \left[ \log \sigma \left( \beta \log \frac{\pi_\theta(s_w|x)}{\pi_{\text{ref}}(s_w|x)} - \beta \log \frac{\pi_\theta(s_l|x)}{\pi_{\text{ref}}(s_l|x)} \right) \right] \quad (9)$$

where  $\mathcal{D}$  denotes the empirical distribution over the constructed preference pairs,  $\sigma(\cdot)$  is the sigmoid function,  $\pi_\theta(s|x)$  is the policy of the model,  $\pi_{\text{ref}}(s|x)$  is the reference policy, and  $\beta$  is the hyperparameter that control the deviation from the base reference policy  $\pi_{\text{ref}}(s|x)$ .

## Medical-Omni post-training

We first curated the Medical-Omni dataset, which consists of 514,668 samples sampled from a pre-trained dataset. The text queries were then transformed into audio using the SpeechT5 model. To increase the diversity of the audio, we employed the SpeechT5 HiFi-GAN Vocoder, a model designed for voice conversion, to modify the audio into different voice styles. This variation in audio styles ensures the model’s ability to generalize across various voice inputs, which is crucial for its performance in real-world applications. The post-training process was carried out on the combined Medical-Omni dataset and the pre-trained dataset with text queries. The mixture of these datasets helps improve the model’s generalization across different input modalities. The post-training was performed for one epoch. During this training, we froze the weights of the vision encoder, the vision MLP, and the language model, updating only the weights of the audio encoder and the audio MLP. For the audio encoder, we utilized a pre-trained model from Intern-Omni, which leverages OpenAI’s open-source Whisper-large-v3 model. This model has been trained on a vast amount of audio data and is known for its robust capabilities in speech recognition and translation.

## Implementation details for external validation

**Dataset curation and evaluation tasks.** For a thorough external validation, we collected CT scans and MRI scans that encompass a range of 11 different diseases across three primary anatomical regions of the human body: HEAD and NECK (including brain tumor, acoustic neuroma, and cerebral hemorrhage), CHEST (lung cancer, pulmonary embolism), and ABDOMEN (bladder cancer, prostate cancer, colon cancer, liver cancer, kidney cancer, pancreatic cancer). Each disease category includes data from 20 patients, all sourced from Sun Yat-sen Memorial Hospital, Sun Yat-sen University. The CT and MRI scans were meticulously annotated by experienced radiologists, who provided detailed segmentation masks for each disease visible in the scans. For the CT scans, we converted the DICOM images into PNG slices, adjusting the window level and window width according to the radiologists’ specifications. For the MRI scans, we directly transformed the DICOM images into PNG slices without additional adjustments. We then extracted the slices containing relevant disease regions and corresponding bounding boxes for the purpose of external evaluation. The final curated dataset consists of a total of 5,981 slices. The specific distribution of these slices for each disease is outlined in Figure 1. This comprehensive dataset ensures a robust external validation of our model across a wide range of diseases and anatomical regions.

The external validation process was carried out on four distinct tasks: (1) multiple-choice question answering, (2) region recognition, (3) lesion detection, and (4) region-based Visual Question Answering (VQA). For the region VQA task, we leveraged Llama-3.1-70B-Instruct [27] to extract sentences from medical reports that aligned with specific regions of interest in the CT and MRI scans. These sentences were then used to construct VQA pairs. In total, 2,760 region VQA test samples were curated for external validation. For the multiple-choice question answering task, the model’s performance was evaluated by calculating the percentage of correct answers. The region recognition task was assessed using the Macro-F1 score, which takes into account both precision and recall to provide a balanced measure of the model’s ability to correctly identify regions of interest. The lesion detection task was evaluated using the Intersection over Union (IoU) metric, which measures the overlap between the predicted lesion regions and the ground truth annotations. For the region VQA task, the generated answers were evaluated using GPT-4o. The evaluation involved scoring the model’s generated responses based on three key factors: (1) the accuracy of the answers, (2) the consistency of the answers with the reference answers, and (3) the clinical relevance of the answers, ensuring that the responses were both correct and contextually meaningful in a clinical setting.

**Implementation for Qualitative comparison of internal and external validation.** We conducted a qualitative comparison of the internal and external validation results to assess the model’s generalization capabilities across different datasets. The internal validation was performed on a held-out set for region recognition and lesion detection, that contains 11 different diseases across four primary anatomical regions: HEAD and NECK, CHEST, ABDOMEN, Pelvic. We compare the qualitative results of region recognition and lesion detection tasks between the internal and external validation datasets.

## Code Availability

The code used in this study will be publicly released after the manuscript is published. Implementation, including network design and training strategies, are given in the Methods section.

## Data Availability

This study incorporates diverse public available biomedical datasets. For detailed information about the data used in this project, please refer to the Appendix.



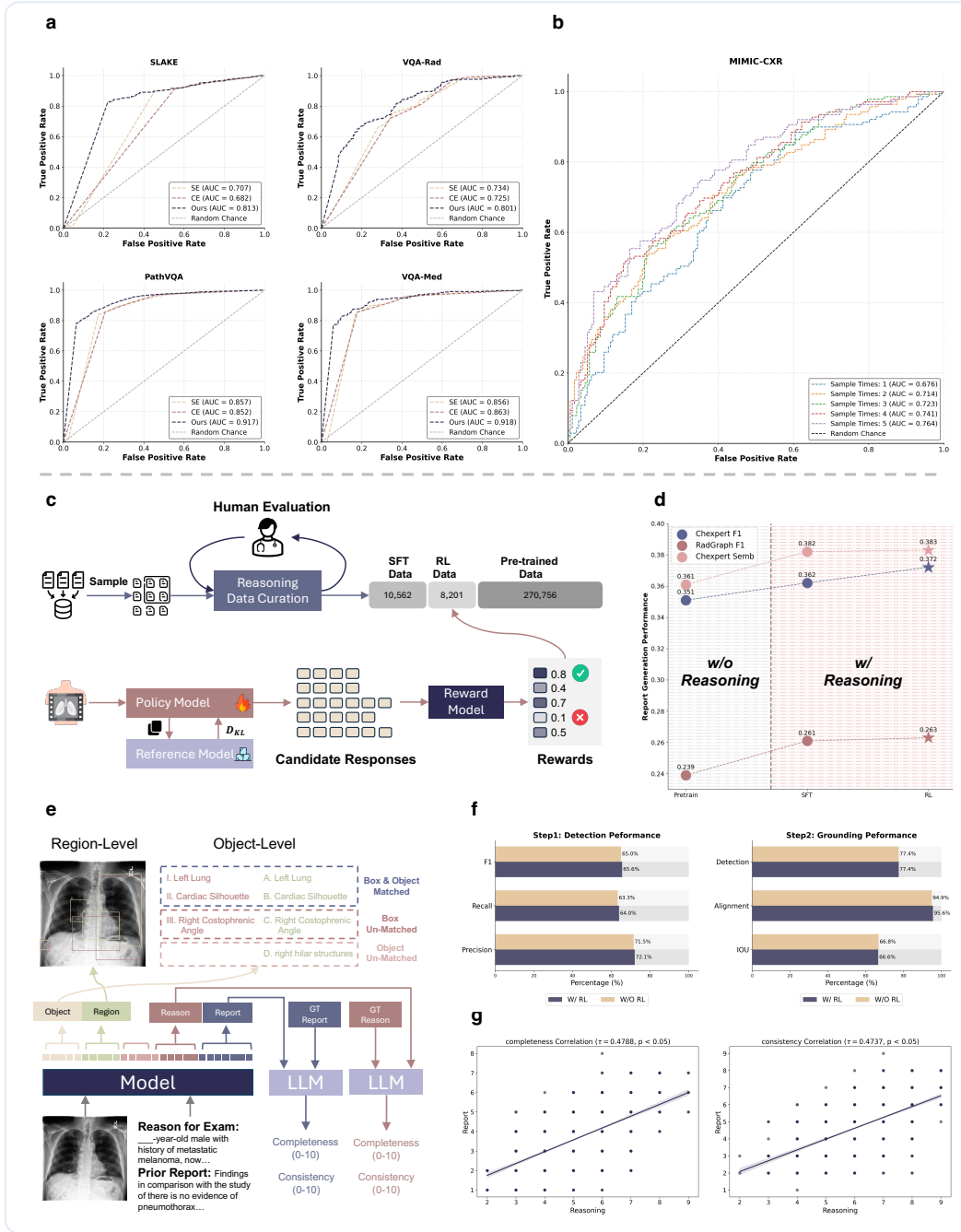


Figure 4: **a**, Comparison of our method with conventional semantic entropy (SE) and discrete entropy (DE) on four VQA tasks using AUROC to assess error prediction. **b**, Performance on image captioning tasks, showing our method AUC improves with more generated questions per sentence. **c**, Overview of curated datasets for supervised fine-tuning (10k samples) and direct preference optimization (8k samples); see Figure 12 and Figure 9 for details. **d**, Impact of long chain-of-thought (CoT) reasoning on clinical captioning tasks, evaluated using CheXpert F1, RadGraph F1, and CheXpert Similarity. **e**, Evaluation protocol for Steps 1, 2, and 4 in CoT: Step 1 and 2 assess region-level, object-level, and alignment performance; Step 4 measures completeness, consistency, and correlation between reasoning and report scores (Kendall Tau). **f**, DPO maintains localization accuracy in Steps 1 and 2 while improve the reasoning reliability and report accuracy. **g**, Improved correlation (Kendall Tau) between reasoning and report quality in Step 4 after applying DPO.

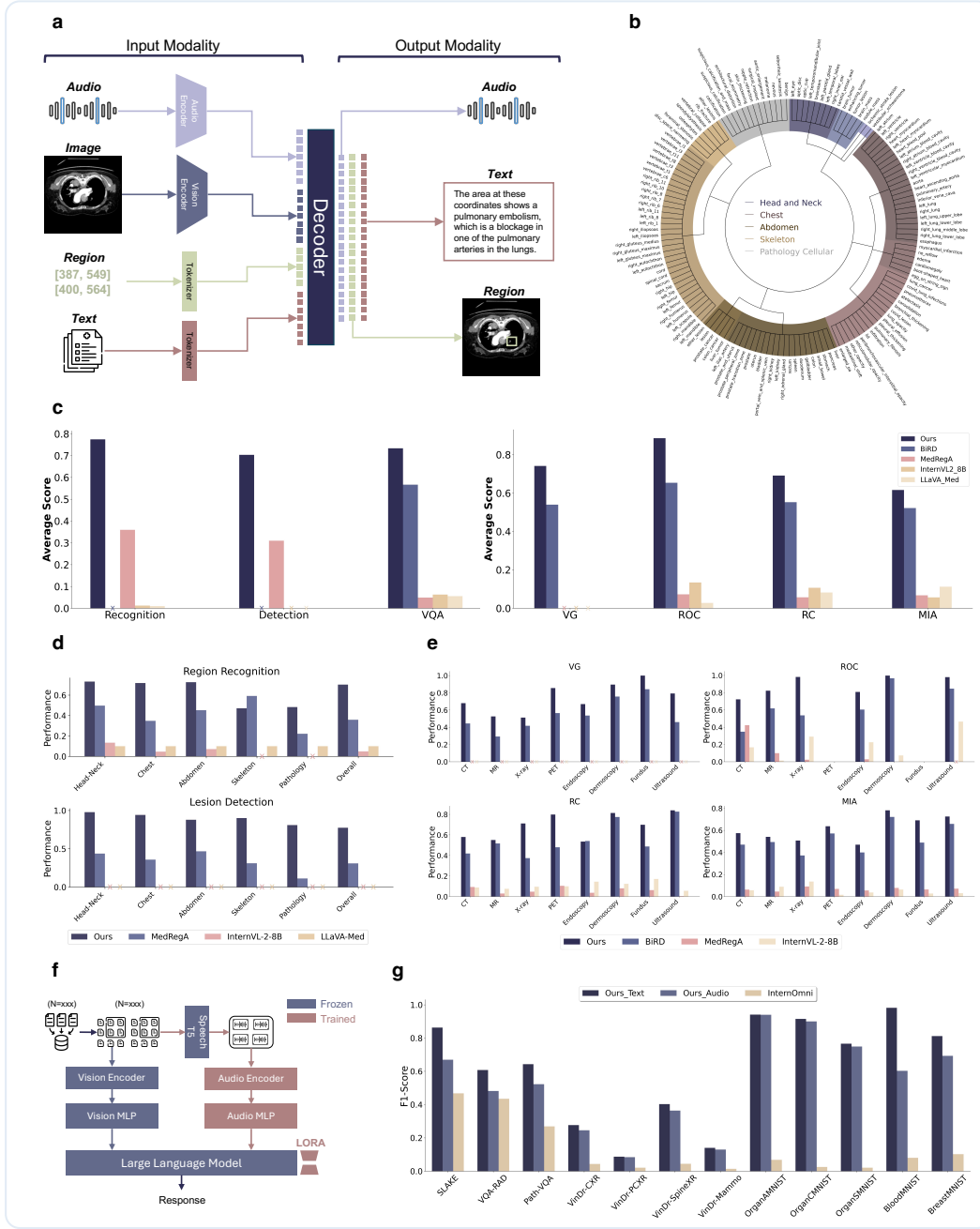


Figure 5: **a**, XMedGPT is an all-in-one biomedical model capable of processing image, text, audio, and region-level inputs, enabling tasks such as region recognition, region-based VQA, and lesion localization. **b**, List of anatomical regions recognizable by XMedGPT, which supports localization of 141 lesion types (see Figure 5b for details). **c**, Performance on region-related tasks: F1-score for region recognition, IoU for lesion localization, and task-specific metrics for Region VQA—acc@0.5 (ROC), SPICE (RC), recall@0.5 (VG), and mBMR (BLEU-2, METEOR, ROUGE-L) for MIA, following the BiRD convention. **d**, Comparative results on region recognition and lesion localization across six anatomical structures. **e**, Performance comparison on Region VQA tasks across eight imaging modalities. **f**, Overview of audio data curation and fine-tuning: 514,668 pretraining instances with audio input were used to update the audio encoder, audio MLP, and LLM (via LoRA), with other components frozen. **g**, Comparison of XMedGPT with audio vs. text inputs and with leading audio models on single-label diagnosis, multi-label diagnosis, and medical VQA tasks.

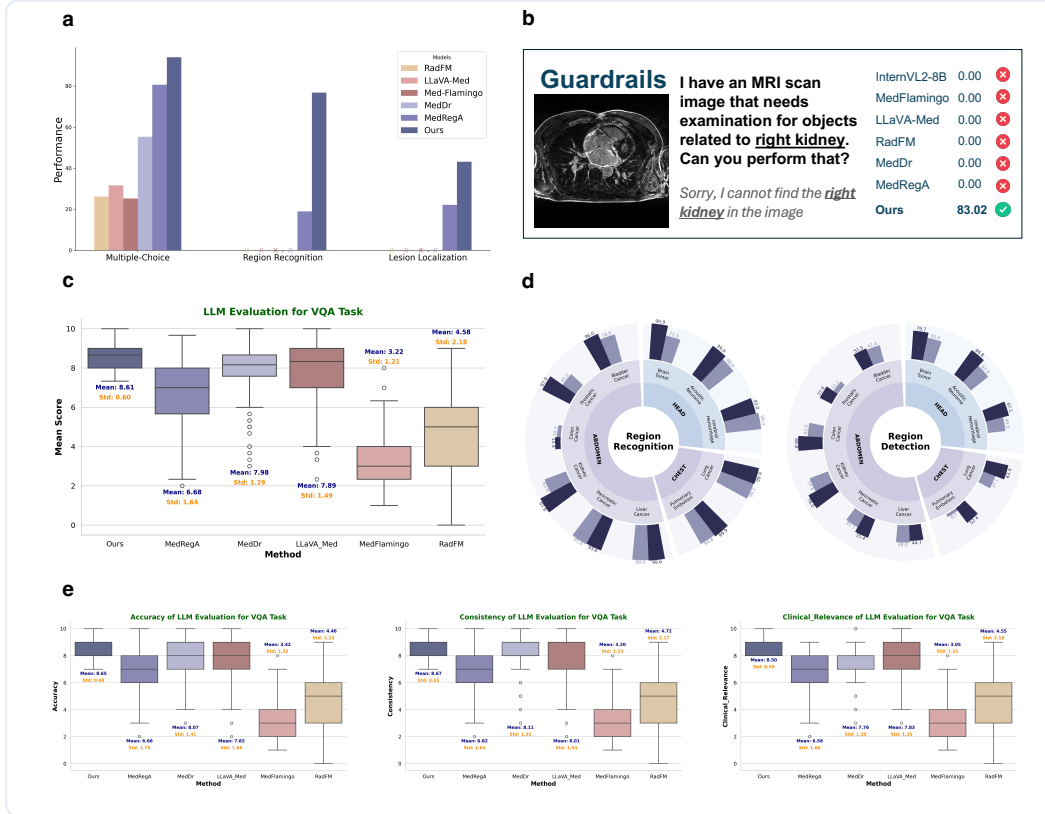


Figure 6: **a**, Evaluation on the external validation data across diverse biomedical tasks (Multiple-choice, Region Recognition and Lesion Localization). Accuracy is used as the evaluation metric for multiple-choice, F1-score is used for region recognition, and Intersection over Union (IoU) is used for lesion localization. **b**, Evaluation of the guardrail capability of XMedGPT and other leading models, with accuracy in detecting unanswerable questions from the provided images used as the evaluation metric. **c**, Results for 11 clinically significant diseases from diverse anatomical regions, evaluated on internal and external datasets. The results demonstrate the generalization performance of XMedGPT on various diseases. **d**, Comparison of XMedGPT with leading models on Region VQA tasks. LLM is used to evaluate the generated free-text from three aspects: accuracy, consistency, and clinical relevance.

## References

- [1] Julián N Acosta, Guido J Falcone, Pranav Rajpurkar, and Eric J Topol. Multimodal biomedical ai. *Nature medicine*, 28(9):1773–1784, 2022.
- [2] Walid Al-Dhabyani, Mohammed Gomaa, Hussien Khaled, and Aly Fahmy. Dataset of breast ultrasound images. *Data in brief*, 28:104863, 2020.
- [3] Michela Antonelli, Annika Reinke, Spyridon Bakas, Keyvan Farahani, Annette Kopp-Schneider, Bennett A Landman, Geert Litjens, Bjoern Menze, Olaf Ronneberger, Ronald M Summers, et al. The medical segmentation decathlon. *Nature communications*, 13(1):4128, 2022.
- [4] Junyi Ao, Rui Wang, Long Zhou, Chengyi Wang, Shuo Ren, Yu Wu, Shujie Liu, Tom Ko, Qing Li, Yu Zhang, et al. Specht5: Unified-modal encoder-decoder pre-training for spoken language processing. *arXiv preprint arXiv:2110.07205*, 2021.
- [5] Guilherme Aresta, Teresa Araújo, Scotty Kwok, Sai Saketh Chennamsetty, Mohammed Safwan, Varghese Alex, Bahram Marami, Marcel Prastawa, Monica Chan, Michael Donovan, et al. Bach: Grand challenge on breast cancer histology images. *Medical image analysis*, 56:122–139, 2019.
- [6] Satanjeev Banerjee and Alon Lavie. Meteor: An automatic metric for mt evaluation with improved correlation with human judgments. In *Proceedings of the acl workshop on intrinsic and extrinsic evaluation measures for machine translation and/or summarization*, pages 65–72, 2005.
- [7] Asma Ben Abacha, Sadid A Hasan, Vivek V Datla, Dina Demner-Fushman, and Henning Müller. Vqa-med: Overview of the medical visual question answering task at imageclef 2019. In *Proceedings of CLEF (Conference and Labs of the Evaluation Forum) 2019 Working Notes*. 9-12 September 2019, 2019.
- [8] Richard J Chen, Tong Ding, Ming Y Lu, Drew FK Williamson, Guillaume Jaume, Andrew H Song, Bowen Chen, Andrew Zhang, Daniel Shao, Muhammad Shaban, et al. Towards a general-purpose foundation model for computational pathology. *Nature Medicine*, 30(3):850–862, 2024.
- [9] Sihong Chen, Kai Ma, and Yefeng Zheng. Med3d: Transfer learning for 3d medical image analysis. *arXiv preprint arXiv:1904.00625*, 2019.
- [10] Zhe Chen, Weiyun Wang, Hao Tian, Shenglong Ye, Zhangwei Gao, Erfei Cui, Wenwen Tong, Kongzhi Hu, Jiapeng Luo, Zheng Ma, et al. How far are we to gpt-4v? closing the gap to commercial multimodal models with open-source suites. *arXiv preprint arXiv:2404.16821*, 2024.
- [11] Zhe Chen, Jiannan Wu, Wenhai Wang, Weijie Su, Guo Chen, Sen Xing, Muyan Zhong, Qinglong Zhang, Xizhou Zhu, Lewei Lu, et al. Internvl: Scaling up vision foundation models and aligning for generic visual-linguistic tasks. In *Proceedings of the IEEE/CVF conference on computer vision and pattern recognition*, pages 24185–24198, 2024.
- [12] Lin Chin-Yew. Rouge: A package for automatic evaluation of summaries. In *Proceedings of the Workshop on Text Summarization Branches Out*, 2004, 2004.
- [13] Matthew Christensen, Milos Vukadinovic, Neal Yuan, and David Ouyang. Vision–language foundation model for echocardiogram interpretation. *Nature Medicine*, 30(5):1481–1488, 2024.
- [14] Marc Combalia, Noel CF Codella, Veronica Rotemberg, Brian Helba, Veronica Vilaplana, Ofer Reiter, Cristina Carrera, Alicia Barreiro, Allan C Halpern, Susana Puig, et al. Bcn20000: Dermoscopic lesions in the wild. *arXiv preprint arXiv:1908.02288*, 2019.
- [15] Donnella S Comeau, Danielle S Bitterman, and Leo Anthony Celi. Preventing unrestricted and unmonitored ai experimentation in healthcare through transparency and accountability. *npj Digital Medicine*, 8(1):42, 2025.

- [16] Adrito Das, Danyal Z Khan, Dimitrios Psychogios, Yitong Zhang, John G Hanrahan, Francisco Vasconcelos, You Pang, Zhen Chen, Jinlin Wu, Xiaoyang Zou, et al. Pitvis-2023 challenge: Workflow recognition in videos of endoscopic pituitary surgery. *arXiv preprint arXiv:2409.01184*, 2024.
- [17] Dina Demner-Fushman, Marc D Kohli, Marc B Rosenman, Sonya E Shooshan, Laritza Rodriguez, Sameer Antani, George R Thoma, and Clement J McDonald. Preparing a collection of radiology examinations for distribution and retrieval. *Journal of the American Medical Informatics Association*, 23(2):304–310, 2016.
- [18] Kexue Deng, Lu Wang, Yuchan Liu, Xin Li, Qiuyang Hou, Mulan Cao, Nathan Norton Ng, Huan Wang, Huanhuan Chen, Kristen W Yeom, et al. A deep learning-based system for survival benefit prediction of tyrosine kinase inhibitors and immune checkpoint inhibitors in stage iv non-small cell lung cancer patients: A multicenter, prognostic study. *EClinicalMedicine*, 51, 2022.
- [19] Reuben Dorent, Aaron Kujawa, Marina Ivory, Spyridon Bakas, Nicola Rieke, Samuel Joutard, Ben Glocker, Jorge Cardoso, Marc Modat, Kayhan Batmanghelich, et al. Crossmoda 2021 challenge: Benchmark of cross-modality domain adaptation techniques for vestibular schwannoma and cochlea segmentation. *Medical Image Analysis*, 83:102628, 2023.
- [20] Sebastian Farquhar, Jannik Kossen, Lorenz Kuhn, and Yarin Gal. Detecting hallucinations in large language models using semantic entropy. *Nature*, 630(8017):625–630, 2024.
- [21] Anahita Fathi Kazerooni, Adam Kraya, Komal S Rath, Meen Chul Kim, Arastoo Vossough, Nastaran Khalili, Ariana M Familiar, Deep Gandhi, Neda Khalili, Varun Keshnerwani, et al. Multiparametric mri along with machine learning predicts prognosis and treatment response in pediatric low-grade glioma. *Nature Communications*, 16(1):340, 2025.
- [22] Huazhu Fu, Fei Li, José Ignacio Orlando, Hrvoje Bogunović, Xu Sun, Jingan Liao, Yanwu Xu, Shaochong Zhang, and Xiulan Zhang. Palm: Pathologic myopia challenge, 2019. URL <https://dx.doi.org/10.21227/55pk-8z03>.
- [23] Jevgenij Gamper, Navid Alemi Koohbanani, Ksenija Benes, Simon Graham, Mostafa Jahanifar, Syed Ali Khurram, Ayesha Azam, Katherine Hewitt, and Nasir Rajpoot. Pannuke dataset extension, insights and baselines. *arXiv preprint arXiv:2003.10778*, 2020.
- [24] Shangqi Gao, Hangqi Zhou, Yibo Gao, and Xiahai Zhuang. Bayeseg: Bayesian modeling for medical image segmentation with interpretable generalizability. *Medical Image Analysis*, 89: 102889, 2023.
- [25] Sergios Gatidis, Tobias Hepp, Marcel Früh, Christian La Fougère, Konstantin Nikolaou, Christina Pfannenberger, Bernhard Schölkopf, Thomas Küstner, Clemens Cyran, and Daniel Rubin. A whole-body fdg-pet/ct dataset with manually annotated tumor lesions. *Scientific Data*, 9(1):601, 2022.
- [26] Peyman Gholami, Priyanka Roy, Mohana Kuppuswamy Parthasarathy, and Vasudevan Lakshminarayanan. Octid: Optical coherence tomography image database. *Computers & Electrical Engineering*, 81:106532, 2020.
- [27] Aaron Grattafiori, Abhimanyu Dubey, Abhinav Jauhri, Abhinav Pandey, Abhishek Kadian, Ahmad Al-Dahle, Aiesha Letman, Akhil Mathur, Alan Schelten, Alex Vaughan, et al. The llama 3 herd of models. *arXiv preprint arXiv:2407.21783*, 2024.
- [28] Paul Hager, Friederike Jungmann, Robbie Holland, Kunal Bhagat, Inga Hubrecht, Manuel Knauer, Jakob Vielhauer, Marcus Makowski, Rickmer Braren, Georgios Kaissis, et al. Evaluation and mitigation of the limitations of large language models in clinical decision-making. *Nature medicine*, 30(9):2613–2622, 2024.
- [29] Sunan He, Yuxiang Nie, Zhixuan Chen, Zhiyuan Cai, Hongmei Wang, Shu Yang, and Hao Chen. Meddr: Diagnosis-guided bootstrapping for large-scale medical vision-language learning. *arXiv preprint arXiv:2404.15127*, 2024.



- [30] Xuehai He, Yichen Zhang, Luntian Mou, Eric Xing, and Pengtao Xie. Pathvqa: 30000+ questions for medical visual question answering. *arXiv preprint arXiv:2003.10286*, 2020.
- [31] Nicholas Heller, Fabian Isensee, Dasha Trofimova, Resha Tejpaul, Zhongchen Zhao, Huai Chen, Lisheng Wang, Alex Golts, Daniel Khapun, Daniel Shats, et al. The kits21 challenge: Automatic segmentation of kidneys, renal tumors, and renal cysts in corticomedullary-phase ct. *arXiv preprint arXiv:2307.01984*, 2023.
- [32] Moritz R Hernandez Petzsche, Ezequiel de la Rosa, Uta Hanning, Roland Wiest, Waldo Valenzuela, Mauricio Reyes, Maria Meyer, Sook-Lei Liew, Florian Kofler, Ivan Ezhov, et al. Isles 2022: A multi-center magnetic resonance imaging stroke lesion segmentation dataset. *Scientific data*, 9(1):762, 2022.
- [33] Yutao Hu, Tianbin Li, Quanfeng Lu, Wenqi Shao, Junjun He, Yu Qiao, and Ping Luo. Omnimed-vqa: A new large-scale comprehensive evaluation benchmark for medical lvlm. In *Proceedings of the IEEE/CVF Conference on Computer Vision and Pattern Recognition*, pages 22170–22183, 2024.
- [34] Xiaoshuang Huang, Haifeng Huang, Lingdong Shen, Yehui Yang, Fangxin Shang, Junwei Liu, and Jia Liu. A refer-and-ground multimodal large language model for biomedicine. In *International Conference on Medical Image Computing and Computer-Assisted Intervention*, pages 399–409. Springer, 2024.
- [35] Aaron Hurst, Adam Lerer, Adam P Goucher, Adam Perelman, Aditya Ramesh, Aidan Clark, AJ Ostrow, Akila Welihinda, Alan Hayes, Alec Radford, et al. Gpt-4o system card. *arXiv preprint arXiv:2410.21276*, 2024.
- [36] Saddam Hussain, Syed Muhammad Anwar, and Muhammad Majid. Segmentation of glioma tumors in brain using deep convolutional neural network. *Neurocomputing*, 282:248–261, 2018.
- [37] Wisdom Ikezogwo, Saygin Seyfioglu, Fatemeh Ghezloo, Dylan Geva, Fatwir Sheikh Mohammed, Pavan Kumar Anand, Ranjay Krishna, and Linda Shapiro. Quilt-1m: One million image-text pairs for histopathology. *Advances in neural information processing systems*, 36: 37995–38017, 2023.
- [38] Jeremy Irvin, Pranav Rajpurkar, Michael Ko, Yifan Yu, Silviana Ciurea-Ilcus, Chris Chute, Henrik Marklund, Behzad Haghighi, Robyn Ball, Katie Shpanskaya, et al. Chexpert: A large chest radiograph dataset with uncertainty labels and expert comparison. In *Proceedings of the AAAI conference on artificial intelligence*, volume 33, pages 590–597, 2019.
- [39] Debesh Jha, Pia H Smedsrud, Michael A Riegler, Pål Halvorsen, Thomas De Lange, Dag Johansen, and Håvard D Johansen. Kvasir-seg: A segmented polyp dataset. In *MultiMedia modeling: 26th international conference, MMM 2020, Daejeon, South Korea, January 5–8, 2020, proceedings, part II* 26, pages 451–462. Springer, 2020.
- [40] Yuanfeng Ji, Haotian Bai, Chongjian Ge, Jie Yang, Ye Zhu, Ruimao Zhang, Zhen Li, Lingyan Zhanng, Wanling Ma, Xiang Wan, et al. Amos: A large-scale abdominal multi-organ benchmark for versatile medical image segmentation. *Advances in neural information processing systems*, 35:36722–36732, 2022.
- [41] Alistair EW Johnson, Tom J Pollard, Seth J Berkowitz, Nathaniel R Greenbaum, Matthew P Lungren, Chih-ying Deng, Roger G Mark, and Steven Horng. Mimic-cxr, a de-identified publicly available database of chest radiographs with free-text reports. *Scientific data*, 6(1):317, 2019.
- [42] Karin Rolanda Jongsma, Martin Sand, and Megan Milota. Why we should not mistake accuracy of medical ai for efficiency. *NPJ Digital Medicine*, 7(1):57, 2024.
- [43] Jakob Nikolas Kather, Cleo-Aron Weis, Francesco Bianconi, Susanne M Melchers, Lothar R Schad, Timo Gaiser, Alexander Marx, and Frank Gerrit Zöllner. Multi-class texture analysis in colorectal cancer histology. *Scientific reports*, 6(1):1–11, 2016.

- [44] A Emre Kavur, N Sinem Gezer, Mustafa Barış, Sinem Aslan, Pierre-Henri Conze, Vladimir Groza, Duc Duy Pham, Soumick Chatterjee, Philipp Ernst, Savaş Özkan, et al. Chaos challenge-combined (ct-mr) healthy abdominal organ segmentation. *Medical image analysis*, 69:101950, 2021.
- [45] Chanwoo Kim, Soham U Gadgil, Alex J DeGrave, Jesutofunmi A Omiye, Zhuo Ran Cai, Roxana Daneshjou, and Su-In Lee. Transparent medical image ai via an image-text foundation model grounded in medical literature. *Nature Medicine*, 30(4):1154–1165, 2024.
- [46] Kristin M Kostick-Quenet. A caution against customized ai in healthcare. *npj Digital Medicine*, 8(1):13, 2025.
- [47] Paras Lakhani, John Mongan, Chinmay Singhal, Quan Zhou, Katherine P Andriole, William F Auffermann, PM Prasanna, Theresa X Pham, Michael Peterson, Peter J Bergquist, et al. The 2021 siim-fisabio-rsna machine learning covid-19 challenge: Annotation and standard exam classification of covid-19 chest radiographs. *Journal of Digital Imaging*, 36(1):365–372, 2023.
- [48] Alain Lalonde, Zhihao Chen, Thomas Decourselle, Abdul Qayyum, Thibaut Pommier, Luc Loris, Ezequiel de La Rosa, Alexandre Cochet, Yves Cottin, Dominique Ginhac, et al. Emidec: a database usable for the automatic evaluation of myocardial infarction from delayed-enhancement cardiac mri. *Data*, 5(4):89, 2020.
- [49] Bennett Landman, Zhoubing Xu, J Igelsias, Martin Styner, T Langerak, and Arno Klein. Miccai multi-atlas labeling beyond the cranial vault-workshop and challenge. In *Proc. MICCAI Multi-Atlas Labeling Beyond Cranial Vault—Workshop Challenge*, volume 5, page 12, 2015.
- [50] Jason J Lau, Soumya Gayen, Asma Ben Abacha, and Dina Demner-Fushman. A dataset of clinically generated visual questions and answers about radiology images. *Scientific data*, 5(1): 1–10, 2018.
- [51] Chunyuan Li, Cliff Wong, Sheng Zhang, Naoto Usuyama, Haotian Liu, Jianwei Yang, Tristan Naumann, Hoifung Poon, and Jianfeng Gao. Llava-med: Training a large language-and-vision assistant for biomedicine in one day. *Advances in Neural Information Processing Systems*, 36, 2024.
- [52] Weixiong Lin, Ziheng Zhao, Xiaoman Zhang, Chaoyi Wu, Ya Zhang, Yanfeng Wang, and Weidi Xie. Pmc-clip: Contrastive language-image pre-training using biomedical documents. In *International Conference on Medical Image Computing and Computer-Assisted Intervention*, pages 525–536. Springer, 2023.
- [53] Geert Litjens, Robert Toth, Wendy Van De Ven, Caroline Hoeks, Sjoerd Kerkstra, Bram Van Ginneken, Graham Vincent, Gwenael Guillard, Neil Birbeck, Jindang Zhang, et al. Evaluation of prostate segmentation algorithms for mri: the promise12 challenge. *Medical image analysis*, 18(2):359–373, 2014.
- [54] Aixiu Liu, Bei Feng, Bing Xue, Bingxuan Wang, Bochao Wu, Chengda Lu, Chenggang Zhao, Chengqi Deng, Chenyu Zhang, Chong Ruan, et al. Deepseek-v3 technical report. *arXiv preprint arXiv:2412.19437*, 2024.
- [55] Bo Liu, Li-Ming Zhan, Li Xu, Lin Ma, Yan Yang, and Xiao-Ming Wu. Slake: A semantically-labeled knowledge-enhanced dataset for medical visual question answering. In *2021 IEEE 18th international symposium on biomedical imaging (ISBI)*, pages 1650–1654. IEEE, 2021.
- [56] Haotian Liu, Chunyuan Li, Qingyang Wu, and Yong Jae Lee. Visual instruction tuning. *Advances in neural information processing systems*, 36:34892–34916, 2023.
- [57] Ming Y Lu, Bowen Chen, Drew FK Williamson, Richard J Chen, Ivy Liang, Tong Ding, Guillaume Jaume, Igor Odintsov, Long Phi Le, Georg Gerber, et al. A visual-language foundation model for computational pathology. *Nature Medicine*, 30(3):863–874, 2024.
- [58] Xiangde Luo, Wenjun Liao, Jianghong Xiao, Jieneng Chen, Tao Song, Xiaofan Zhang, Kang Li, Dimitris N Metaxas, Guotai Wang, and Shaoting Zhang. Word: A large scale dataset, benchmark and clinical applicable study for abdominal organ segmentation from ct image. *Medical Image Analysis*, 82:102642, 2022.

- [59] Mojtaba Masoudi, Hamid-Reza Pourreza, Mahdi Saadatmand-Tarzjan, Noushin Eftekhari, Fateme Shafiee Zargar, and Masoud Pezeshki Rad. A new dataset of computed-tomography angiography images for computer-aided detection of pulmonary embolism. *Scientific Data*, 5 (180180), 2018.
- [60] Christian Matek, Sebastian Krappe, Christian Münzenmayer, Torsten Haferlach, and Carsten Marr. Highly accurate differentiation of bone marrow cell morphologies using deep neural networks on a large image data set. *Blood, The Journal of the American Society of Hematology*, 138(20):1917–1927, 2021.
- [61] Md Ashraful Alam Milton. Automated skin lesion classification using ensemble of deep neural networks in isic 2018: Skin lesion analysis towards melanoma detection challenge. *arXiv preprint arXiv:1901.10802*, 2019.
- [62] Abdul Sami Mohammed, Ahmed Abul Hasanaath, Ghazanfar Latif, and Abul Bashar. Knee osteoarthritis detection and severity classification using residual neural networks on preprocessed x-ray images. *Diagnostics*, 13(8):1380, 2023.
- [63] Michael Moor, Qian Huang, Shirley Wu, Michihiro Yasunaga, Yash Dalmia, Jure Leskovec, Cyril Zakka, Eduardo Pontes Reis, and Pranav Rajpurkar. Med-flamingo: a multimodal medical few-shot learner. In *Machine Learning for Health (ML4H)*, pages 353–367. PMLR, 2023.
- [64] Luis Filipe Nakayama, David Restrepo, João Matos, Lucas Zago Ribeiro, Fernando Korn Malerbi, Leo Anthony Celi, and Caio Saito Regatieri. Brset: a brazilian multilabel ophthalmological dataset of retina fundus photos. *PLOS Digital Health*, 3(7):e0000454, 2024.
- [65] Ha Q Nguyen, Khanh Lam, Linh T Le, Hieu H Pham, Dat Q Tran, Dung B Nguyen, Dung D Le, Chi M Pham, Hang TT Tong, Diep H Dinh, et al. Vindr-cxr: An open dataset of chest x-rays with radiologist’s annotations. *Scientific Data*, 9(1):429, 2022.
- [66] Hieu T Nguyen, Hieu H Pham, Nghia T Nguyen, Ha Q Nguyen, Thang Q Huynh, Minh Dao, and Van Vu. Vindr-spinexr: A deep learning framework for spinal lesions detection and classification from radiographs. In *Medical Image Computing and Computer Assisted Intervention–MICCAI 2021: 24th International Conference, Strasbourg, France, September 27–October 1, 2021, Proceedings, Part V 24*, pages 291–301. Springer, 2021.
- [67] Hieu T Nguyen, Ha Q Nguyen, Hieu H Pham, Khanh Lam, Linh T Le, Minh Dao, and Van Vu. Vindr-mammo: A large-scale benchmark dataset for computer-aided diagnosis in full-field digital mammography. *Scientific Data*, 10(1):277, 2023.
- [68] Andre GC Pacheco, Gustavo R Lima, Amanda S Salomao, Breno Krohling, Igor P Biral, Gabriel G de Angelo, Fábio CR Alves Jr, José GM Esgario, Alana C Simora, Pedro BC Castro, et al. Pad-ufes-20: A skin lesion dataset composed of patient data and clinical images collected from smartphones. *Data in brief*, 32:106221, 2020.
- [69] Suraj Pai, Dennis Bontempi, Ibrahim Hadzic, Vasco Prudente, Mateo Sokač, Tafadzwa L Chaunzwa, Simon Bernatz, Ahmed Hosny, Raymond H Mak, Nicolai J Birkbak, et al. Foundation model for cancer imaging biomarkers. *Nature machine intelligence*, 6(3):354–367, 2024.
- [70] Sachin Panchal, Ankita Naik, Manesh Kokare, Samiksha Pachade, Rushikesh Naigaonkar, Prerana Phadnis, and Archana Bhange. Retinal fundus multi-disease image dataset (rfmid) 2.0: a dataset of frequently and rarely identified diseases. *Data*, 8(2):29, 2023.
- [71] Kishore Papineni, Salim Roukos, Todd Ward, and Wei-Jing Zhu. Bleu: a method for automatic evaluation of machine translation. In *Proceedings of the 40th annual meeting of the Association for Computational Linguistics*, pages 311–318, 2002.
- [72] H Hieu Pham, T Thanh Tran, and Ha Quy Nguyen. Vindr-pcxr: An open, large-scale pediatric chest x-ray dataset for interpretation of common thoracic diseases. *PhysioNet (version 1.0. 0)*, 10(2), 2022.
- [73] Pranav Rajpurkar, Jeremy Irvin, Aarti Bagul, Daisy Ding, Tony Duan, Hershel Mehta, Brandon Yang, Kaylie Zhu, Dillon Laird, Robyn L Ball, et al. Mura: Large dataset for abnormality detection in musculoskeletal radiographs. *arXiv preprint arXiv:1712.06957*, 2017.

- [74] Pranav Rajpurkar, Emma Chen, Oishi Banerjee, and Eric J Topol. Ai in health and medicine. *Nature medicine*, 28(1):31–38, 2022.
- [75] Vishwanatha M Rao, Michael Hla, Michael Moor, Subathra Adithan, Stephen Kwak, Eric J Topol, and Pranav Rajpurkar. Multimodal generative ai for medical image interpretation. *Nature*, 639(8056):888–896, 2025.
- [76] Eduardo Pontes Reis, Felipe Nascimento, Mateus Aranha, Fernando Mainetti Secol, Birajara Machado, Marcelo Felix, Anouk Stein, and Edson Amaro. Brain hemorrhage extended (bhx): Bounding box extrapolation from thick to thin slice ct images. *PhysioNet*, 101(23):e215–20, 2020.
- [77] Blaine Rister, Darvin Yi, Kaushik Shivakumar, Tomomi Nobashi, and Daniel L Rubin. Ct-org, a new dataset for multiple organ segmentation in computed tomography. *Scientific Data*, 7(1): 381, 2020.
- [78] Amber L Simpson, Michela Antonelli, Spyridon Bakas, Michel Bilello, Keyvan Farahani, Bram Van Ginneken, Annette Kopp-Schneider, Bennett A Landman, Geert Litjens, Bjoern Menze, et al. A large annotated medical image dataset for the development and evaluation of segmentation algorithms. *arXiv preprint arXiv:1902.09063*, 2019.
- [79] Akshay Smit, Saahil Jain, Pranav Rajpurkar, Anuj Pareek, Andrew Y Ng, and Matthew P Lungren. Chexbert: combining automatic labelers and expert annotations for accurate radiology report labeling using bert. *arXiv preprint arXiv:2004.09167*, 2020.
- [80] Lehan Wang, Haonan Wang, Honglong Yang, Jiaji Mao, Zehong Yang, Jun Shen, and Xiaomeng Li. Interpretable bilingual multimodal large language model for diverse biomedical tasks. *arXiv preprint arXiv:2410.18387*, 2024.
- [81] Peng Wang, Shuai Bai, Sinan Tan, Shijie Wang, Zhihao Fan, Jinze Bai, Keqin Chen, Xuejing Liu, Jialin Wang, Wenbin Ge, et al. Qwen2-vl: Enhancing vision-language model’s perception of the world at any resolution. *arXiv preprint arXiv:2409.12191*, 2024.
- [82] Shuo Wang, Chen Qin, Chengyan Wang, Kang Wang, Haoran Wang, Chen Chen, Cheng Ouyang, Xutong Kuang, Chengliang Dai, Yuanhan Mo, Zhang Shi, Chenchen Dai, Xinrong Chen, He Wang, and Wenjia Bai. The extreme cardiac mri analysis challenge under respiratory motion (cmrxmotion), 2022.
- [83] Jakob Wasserthal, Hanns-Christian Breit, Manfred T Meyer, Maurice Pradella, Daniel Hinck, Alexander W Sauter, Tobias Heye, Daniel T Boll, Joshy Cyriac, Shan Yang, et al. Totalsegmentator: robust segmentation of 104 anatomic structures in ct images. *Radiology: Artificial Intelligence*, 5(5):e230024, 2023.
- [84] Chaoyi Wu, Xiaoman Zhang, Ya Zhang, Yanfeng Wang, and Weidi Xie. Towards generalist foundation model for radiology. *arXiv preprint arXiv:2308.02463*, 2023.
- [85] Joy T Wu, Nkechinyere N Agu, Ismini Lourentzou, Arjun Sharma, Joseph A Paguio, Jasper S Yao, Edward C Dee, William Mitchell, Satyananda Kashyap, Andrea Giovannini, et al. Chest imagenome dataset for clinical reasoning. *arXiv preprint arXiv:2108.00316*, 2021.
- [86] Junde Wu, Huihui Fang, Fei Li, Huazhu Fu, Fengbin Lin, Jiongcheng Li, Yue Huang, Qinji Yu, Sifan Song, Xinxing Xu, et al. Gamma challenge: glaucoma grading from multi-modality images. *Medical Image Analysis*, 90:102938, 2023.
- [87] Jinxi Xiang, Xiyue Wang, Xiaoming Zhang, Yinghua Xi, Feyisope Eweje, Yijiang Chen, Yuchen Li, Colin Bergstrom, Matthew Gopaulchan, Ted Kim, et al. A vision–language foundation model for precision oncology. *Nature*, pages 1–10, 2025.
- [88] Jiancheng Yang, Rui Shi, Donglai Wei, Zequan Liu, Lin Zhao, Bilian Ke, Hanspeter Pfister, and Bingbing Ni. Medmnist v2-a large-scale lightweight benchmark for 2d and 3d biomedical image classification. *Scientific Data*, 10(1):41, 2023.

- [89] Jin Ye, Junlong Cheng, Jianpin Chen, Zhongying Deng, Tianbin Li, Haoyu Wang, Yanzhou Su, Ziyang Huang, Jilong Chen, Lei Jiang, et al. Sa-med2d-20m dataset: Segment anything in 2d medical imaging with 20 million masks. *arXiv preprint arXiv:2311.11969*, 2023.
- [90] Jin Ye, Guoan Wang, Yanjun Li, Zhongying Deng, Wei Li, Tianbin Li, Haodong Duan, Ziyang Huang, Yanzhou Su, Benyou Wang, et al. Gmai-mmbench: A comprehensive multimodal evaluation benchmark towards general medical ai. *Advances in Neural Information Processing Systems*, 37:94327–94427, 2024.
- [91] Kai Zhang, Rong Zhou, Eashan Adhikarla, Zhiling Yan, Yixin Liu, Jun Yu, Zhengliang Liu, Xun Chen, Brian D Davison, Hui Ren, et al. A generalist vision–language foundation model for diverse biomedical tasks. *Nature Medicine*, pages 1–13, 2024.
- [92] Minghui Zhang, Yangqian Wu, Hanxiao Zhang, Yulei Qin, Hao Zheng, Wen Tang, Corey Arnold, Chenhao Pei, Pengxin Yu, Yang Nan, et al. Multi-site, multi-domain airway tree modeling. *Medical image analysis*, 90:102957, 2023.
- [93] Sheng Zhang, Yanbo Xu, Naoto Usuyama, Hanwen Xu, Jaspreet Bagga, Robert Tinn, Sam Preston, Rajesh Rao, Mu Wei, Naveen Valluri, et al. A multimodal biomedical foundation model trained from fifteen million image–text pairs. *NEJM AI*, 2(1):AIoa2400640, 2025.
- [94] Xiaoman Zhang, Chaoyi Wu, Ziheng Zhao, Weixiong Lin, Ya Zhang, Yanfeng Wang, and Weidi Xie. Pmc-vqa: Visual instruction tuning for medical visual question answering. *arXiv preprint arXiv:2305.10415*, 2023.
- [95] Yukun Zhou, Mark A Chia, Siegfried K Wagner, Murat S Ayhan, Dominic J Williamson, Robbert R Struyven, Timing Liu, Moucheng Xu, Mateo G Lozano, Peter Woodward-Court, et al. A foundation model for generalizable disease detection from retinal images. *Nature*, 622(7981):156–163, 2023.



## Appendix

### Training Datasets

#### Image Captioning

**PMC-OA** [52] is a biomedical dataset with 1.6M image-caption pairs collected from PubMedCentral’s OpenAccess subset which covers diverse modalities or diseases. We leveraged the dataset for alignment training.

**QUILT** [37] is a large-scale vision-language dataset consisting of 802,144 image and text pairs, which was curated from video frames and corresponding subtitles on YouTube. We leveraged the dataset for alignment training.

#### Visual Question Answering

**SLAKE** [55] is a bilingual radiology VQA dataset consists of 642 radiology images and over 7000 diverse QA pairs annotated by experienced physicians. Following the official split, we used both English and Chinese versions for training, which contains 4919 and 4916 question-answer pairs respectively.

**VQA-RAD** [50] consists of 3.5K question-answering pairs on 314 radiology images, where clinicians asked naturally occurring questions about radiology images and provided reference answers. Following the official split, we use 3,064 question-answer pairs for training.

**PathVQA** [30] consists of 32,799 open-ended questions from 4,998 pathology images where each question is manually checked to ensure correctness. Every image is paired with several questions related to multiple aspects such as shape, color and location. Following the official split, we use 19,755 question-answer pairs for training.

**PMC-VQA** [94] consists of 1.6 million question-answer pairs, which is a large-scale medical visual question-answering dataset generated from PMC-OA. We combined two versions of PMC-VQA and use 329,551 question-answer pairs for training.

**MedPix** is collected from MedPix website<sup>2</sup>, which is a free open-access online database for medical usage. RadFM [84] separate the dataset into MPx-single and MPx-multi. We apply the MPx-single part and use 92,282 question-answer pairs for training.

#### Report Generation

**MIMIC-CXR** [41] is a large-scale chest image-report dataset that consists of 371,920 chest X-rays associated with 227,943 reports from 65,079 patients. Following RadFM [84], we use 354,569 cases for training.

**IU-Xray** [17] consists of 7,470 images and 3,955 reports collected from the Indiana Network. Following MedRegA [80], we use 4,720 cases for training.

#### Medical Image Classification

**VinDr-CXR** [65] consists of 18,000 images that were manually annotated by a total of 17 experienced radiologists with 22 local labels of rectangles surrounding abnormalities and 6 global labels of suspected diseases. The training set contains 15,000 scans, and 3 radiologists independently label each image. Following the official split, we use 45,000 samples for training.

**VinDr-PCXR** [72] is a pediatric CXR dataset of 9,125 studies that were retrospectively collected from a major pediatric hospital in Vietnam between 2020-2021. Each scan was manually annotated by an experienced radiologist for the presence of 36 critical findings and 15 diseases. Following the official split, we use 4,585 samples for training.

**VinDr-SpineXR** [66] is a large-scale annotated medical image dataset for spinal lesion detection and classification from radiographs. The dataset contains 10,466 spine X-ray images from 5,000 studies, each of which is manually annotated with 13 types of abnormalities by an experienced radiologist

---

<sup>2</sup> <https://medpix.nlm.nih.gov>

with bounding boxes around abnormal findings. Following RadFM [84], we use 8,389 samples for training.

**VinDr-Mammo** [67] is a large-scale full-field digital mammography dataset of 5,000 four-view exams. Following the official split, we use 16,391 samples for training.

**CheXpert** [38] is a large public dataset for chest radiograph interpretation, which retrospectively collected the chest from Stanford Hospital, performed between October 2002 and July 2017. The dataset contains 224,316 chest radiographs of 65,240 patients. Following the official split, we use 223,414 samples for training.

**MURA** [73] is a large-scale dataset of musculoskeletal radiographs containing 40,561 images from 14,863 studies, where each study is manually labeled by radiologists as either normal or abnormal. Following the official split, we use 36,808 samples for training.

**ISIC2018** [61] is a skin lesion dataset acquired with 7 dermatoscope types. Following the official split, we use 10,015 samples for training.

**ISIC2019** [14] is a skin lesion dataset labeled with 8 different categories. Following the official split, we use 25,331 samples for training.

**PAD-UFES** [68] is a skin lesion dataset composed of clinical images collected from smartphone devices and a set of patient clinical data containing up to 22 features. The dataset consists of 1,373 patients, 1,641 skin lesions, and 2,298 images for six different diagnostics. We randomly sample 80% of the dataset for training, which includes 1,838 samples.

**Kather colon dataset** [43] is a dataset of 100,000 non-overlapping image patches from hematoxylin & eosin (H&E) stained histological images of human colorectal cancer (CRC) and normal tissue, covering 9 tissue classes in total.

**BRSET** [64] is a multi-labeled ophthalmological dataset consisting of 16,266 images from 8,524 Brazilian patients. Multi-labels are included alongside color fundus retinal photos. We randomly sample 80% of the dataset for training, containing 13,012 samples.

**ODIR-5K**<sup>3</sup> is a structured ophthalmic database of 5,000 patients with age, color fundus photographs from left and right eyes and doctors' diagnostic keywords from doctors. Following the official split, we use 6,392 samples for training.

**OCT2017**<sup>4</sup> includes 83,484 OCT images of 4,686 patients, consisting of 4 categories, normal, drusen, choroidal neoVascularisation (CNV), and Diabetic Macular Edema (DME). Following the official split, we use 82,484 samples for training.

**Butterfly Network ultrasound dataset**<sup>5</sup> is a large dataset containing 9 different classes of ultrasound images acquired with the Butterfly IQ on 31 individuals. Following MedRegA [80], 34,325 images are applied for training.

**BUSI** [2] includes breast ultrasound images among women between 25 and 75 years old. The number of patients is 600 females, patients. The dataset consists of 780 images that are categorized into three classes, namely, standard, benign, and malignant. We randomly sample 80% of the dataset for training, which includes 630 images.

### Region-centric Dataset

**SA-Med2D-20M** [89] is a large-scale segmentation dataset of 2D medical images built upon numerous public and private datasets. The dataset consists of 4.6 million 2D medical images and 19.7 million corresponding masks, covering almost the whole body and showing significant diversity. We filter approximately 285K images from the original dataset, and construct 242,268 and 229,340 training samples for Region-to-Text Identification and Text-to-Region Detection respectively.

**VinDr Series Dataset** is a large-scale classification composed of VinDr-CXR, VinDr-PCXR, VinDr-SpineXR, VinDr-Mammo. The datasets provide radiologist's bounding-box annotation for abnormal areas. We follow the official split and apply the samples with bounding boxes.

<sup>3</sup> <https://odir2019.grand-challenge.org/>

<sup>4</sup> <https://www.kaggle.com/paultimothymooneylkermany2018>.

<sup>5</sup> <https://github.com/ButterflyNetwork/MITGrandHack2018>

**ISIC Challenge Dataset** contains lesion segmentation data where the original image is paired with manually annotated lesion boundaries. We follow the official split and convert the segmentation map into bounding boxes.

**PanNuke** [23] is a semi-automatically generated nuclei instance segmentation dataset. We follow the official split and convert the segmentation map into bounding boxes to formulate region-text pairs.

**Chest-ImaGenome** [85] applied a CXR bounding box detection pipeline to automatically label frontal chest x-ray images from MIMIC-CXR dataset with 29 annotations, from which we selected 12 standardized structures in the chest. Following the split of MIMIC-CXR in RadFM [84], we filtered the chest x-ray scans paired with annotation boxes, and obtained 222,588 samples for training.

**MM-WHS** [24] (Multi-Modality Whole Heart Segmentation) is a challenge of MICCAI 2017 with a dataset of 120 multimodal cardiac images, including 60 cardiac CT/CTA and 60 cardiac MRI images.

**MSD Pancreas** [3] aims to segment the pancreas and tumours from CT images. MSD chose this dataset due to label imbalance, which includes large (background), medium (pancreas), and small (tumour) structures. The dataset comprises 420 cases of 3D CT data, officially split into 281 training cases and 139 test cases. This dataset includes three types of pancreatic tumours: intraductal papillary mucinous neoplasm, pancreatic neuroendocrine tumour, and pancreatic ductal adenocarcinoma.

**MSD Colon Cancer** [3] aims to segment colon tumours from CT images. The reason MSD chose this dataset is due to the challenges posed by heterogeneous appearances and the difficulties in annotation. The dataset includes portal vein CT scans of 190 patients who underwent resection surgery for primary colon cancer, and is officially divided into 126 training cases and 64 testing cases.

**GAMMA** [86] consists of 2D fundus images and 3D optical coherence tomography (OCT) images of 300 patients. The dataset was annotated with glaucoma grade in every sample, and macular fovea coordinates as well as optic disc/cup segmentation mask in the fundus image.

**PathMNIST** [88] is for predicting survival from colorectal cancer histology slides, providing a dataset (NCT-CRC-HE-100K) of 100000 non-overlapping image patches from hematoxylin & eosin stained histological images, and a test dataset (CRC-VAL-HE-7K) of 7180 image patches from a different clinical center.

**ChestMNIST** [88] is a dataset comprising 112120 frontal-view X-Ray images of 30805 unique patients with the text-mined 14 disease labels, which could be formulized as a multi-label binary-class classification task. We use the official data split, and resize the source images of  $1 \times 1024 \times 1024$  into  $1 \times 28 \times 28$ .

**DermaMNIST** [88] consists of 10015 dermatoscopic images categorized as 7 different diseases, formulized as a multi-class classification task. We split the images into training, validation and test set with a ratio of 7 : 1 : 2. The source images of  $3 \times 600 \times 450$  are resized into  $3 \times 28 \times 28$ .

**OCTMNIST** [88] is comprised of 4 diagnosis categories, leading to a multi-class classification task. We split the source training set with a ratio of 9 : 1 into training and validation set, and use its source validation set as the test set. The source images are gray-scale, and their sizes are (384-1536) (277-512). We center-crop the images with a window size of length of the short edge and resize them into  $1 \times 28 \times 28$ .

**OrganA,C,SMNIST** [88] is based on 3D computed tomography (CT) images from Liver Tumor Segmentation Benchmark. They are renamed from OrganMNIST (in MedMNIST v19) for simplicity. We use bounding box annotations of 11 body organs from another study [30] to obtain the organ labels. Hounsfield-Unit (HU) of the 3D images are transformed into gray-scale with an abdominal window. We crop 2D images from the center slices of the 3D bounding boxes in axial / coronal / sagittal views (planes). The only differences of OrganA,C,SMNIST are the views. The images are resized into  $1 \times 28 \times 28$  to perform multi-class classification of 11 body organs. 115 and 16 CT scans from the source training set are used as training and validation set, respectively. The 70 CT scans from the source test set are treated as the test set.

**PneumoniaMNIST** [88] consists of 5856 pediatric chest X-Ray images. The task is binary-class classification of pneumonia against normal. We split the source training set with a ratio of 9 : 1 into training and validation set, and use its source validation set as the test set. The source images are gray-scale, and their sizes are (384-2916) (127-2713). We center-crop the images with a window size of length of the short edge and resize them into  $1 \times 28 \times 28$ .

**RetinaMNIST** [88] provides a dataset of 1600 retina fundus images. The task is ordinal regression for 5-level grading of diabetic retinopathy severity. We split the source training set with a ratio of 9 : 1 into training and validation set, and use the source validation set as the test set. The source images of 3 1736 1824 are center-cropped with a window size of length of the short edge and resized into  $3 \times 28 \times 28$ .

**BreastMNIST** [88] is categorized into 3 classes: normal, benign, and malignant. As we use low-resolution images, we simplify the task into binary classification by combining normal and benign as positive and classifying them against malignant as negative. We split the source dataset with a ratio of 7 : 1 : 2 into training, validation and test set. The source images of 1 500 500 are resized into  $1 \times 28 \times 28$ .

**BloodMNIST** [88] is a dataset of individual normal cells, captured from individuals without infection, hematologic or oncologic disease and free of any pharmacologic treatment at the moment of blood collection. It contains a total of 17,092 images and is organized into 8 classes. We split the source dataset with a ratio of 7 : 1 : 2 into training, validation and test set. The source images with resolution  $3 \times 360 \times 360$  pixels are center-cropped into  $3 \times 200 \times 200$ , and then resized into  $3 \times 28 \times 28$ .

**TissueMNIST** [88] contains 236386 human kidney cortex cells, segmented from 3 reference tissue specimens and organized into 8 categories. We split the source dataset with a ratio of 7 : 1 : 2 into training, validation and test set. Each gray-scale image is  $32 \times 32 \times 7$  pixels, where 7 denotes 7 slices. We obtain 2D maximum projections by taking the maximum pixel value along the axial-axis of each pixel, and resize them into  $28 \times 28$  gray-scale images.

**BTCV**<sup>6</sup> A total of 50 abdominal CT scans were included, which were derived from patients with metastatic liver cancer or postoperative abdominal wall hernias. Each scan of the dataset was performed during the portal vein contrast phase with different volume and field of view parameters. The in-plane resolution in the dataset varies from  $0.54 \times 0.54 \text{ mm}^2$  to  $0.98 \times 0.98 \text{ mm}^2$ , and the slice thickness ranges from 2.5 mm to 5.0 mm.

**AutoPET** [25] is a large-scale PET/CT image dataset focused on whole-body tumour segmentation. The training set consisted of 1014 paired PET-CT images of 900 patients, and the test set consisted of 200 images. Each case data consists of a 3D whole-body FDG-PET image, a 3D whole-body CT image, and a manually annotated 3D tumour mask.

**Knee Osteoarthritis** [62] contains knee X-ray data for knee testing and Kellgren–Lawrence grading. A total of 9786 images of the knee are classified into 5 severity levels according to the Kellgren–Lawrence (KL) grading system: 0 (healthy), 1 (suspicious), 2 (mild), 3 (moderate), and 4 (severe). All images have a resolution of  $224 \times 224$  pixels. About 40% of the dataset images fall into the health category, while the proportion of suspicious images is about 18%, the proportion of minimal images is 26%, the proportion of medium images is 13%, and the proportion of severe images is just over 3%.

**CHAOS** [44] is one of the classic benchmarks for abdominal medical image segmentation, and its biggest feature is that it provides pairs of multimodal CT and MR data and provides corresponding annotations. The CHAOS dataset was released in the ISBI 2019 Challenge, with a total of 40 paired CT and MR data, of which only 20 were annotated as training sets.

**MSD Lung Tumours** [78] aims to segment lung tumours from CT images, and MSD chose this dataset because of "segmenting small targets in a large background". The dataset contains thin-slice CT scans of 96 patients with non-small cell lung cancer, which is officially divided into 64 training sets and 32 test sets.

**ChestX-ray14** is a medical imaging dataset that contains 112,120 frontal view X-ray images from 30,805 patients, collected from 1992 to 2015. The dataset extracted labels for 14 common diseases from radiology reports using Natural Language Processing (NLP) techniques, including atelectasis, infiltration, pneumothorax, edema, emphysema, fibrosis, effusion, pneumonia, pleural thickening, cardiomegaly, nodules, masses, and hernia.

**AMOS** [40] provides 500 CT and 100 MR scans from multi-centre, multi-vendor, multi-modal, multi-period, multi-disease patients, each with voxel-level annotations for 15 abdominal organs. Compared

<sup>6</sup> <https://www.synapse.org/Synapse:syn3193805/wiki/89480>

with the previous medical image analysis datasets, AMOS provides fine annotation of up to 15 abdominal organs while ensuring a large amount of data, which has high clinical value.

**EMIDEC** [48] is a dataset designed to assess the extent of myocardial infarction. The dataset collected delayed-enhanced magnetic resonance imaging (DE-MRI) images of multiple patients a few minutes after contrast injection, and manually annotated multiple myocardial infarction-related regions, including myocardial contours, infarct areas, and permanent microvascular occlusion areas (areas without reflux), to form a segmented dataset. The dataset contains data on 150 patients (all from different patients), of which 50 were normal MRI imaging after contrast media injection and 100 were myocardial infarction (showing areas of high enhancement on DE-MRI). The dataset contains 100 training sets and 50 test sets.

**Kvasir-SEG** [39] is an endoscopic dataset for pixel-level segmentation of colon polyps, which includes 1000 images of gastrointestinal polyps and their corresponding segmentation masks, which are personally annotated and verified by senior gastroenterologists. The official data warehouse provides a breakdown of training and validation data at a ratio of 880:120.

**MSD Hepatic Vessel** [78] aims to segment liver vessels and tumours from liver CT, and MSD chose this dataset because of "the nature of hepatic blood vessels that are adjacent, tubular and interconnected to heterogeneous tumours." The dataset contains 443 3D CT data, divided into 303 training sets and 140 test sets.

**WORD** [58] is a large-scale abdominal organ segmentation CT dataset. The dataset includes 150 CT scans that provide comprehensive coverage of the abdominal region and provide detailed annotations for 16 different abdominal organs. Officially, this data is divided into 100 for training, 20 for validation, and 30 for testing.

**KiTS23** [31] focuses on CT segmentation of the kidney and tumours and cysts on it. The dataset includes 599 cases, of which 489 were used for training and 110 for testing.

**OCTUD** [26] contains over 500 high-resolution images categorized into different pathological conditions. The image classes include Normal (NO), Macular Hole (MH), Age-related Macular Degeneration (AMD), Central Serous Retinopathy (CSR), and Diabetic Retinopathy (DR).

**ICIAR** [5] contains a total of 400 microscope images distributed as follows: normal: 100, benign: 100, carcinoma in situ: 100, invasive carcinoma: 100 and performs two tasks: Automatically classify H&E-stained breast histology microscopy images into four categories: normal, benign, carcinoma in situ, and invasive carcinoma and Perform pixel-level tagging on the entire slice image in the same four categories..

**VQA-Med** [7] contains four main question categories: Modality, Plane, Organ System, and Abnormality. It contains a total of 4,200 radiology images and their corresponding 15,292 question-answer pairs, divided into a training set of 3,200 images and 12,792 question-answer pairs, a validation set of 500 images and 2,000 question-answer pairs, and a test set of 500 images and 500 questions.

**CrossMoDA** [19] is a large and multi-class benchmark for unsupervised cross-modality Domain Adaptation. The goal of the challenge is to segment two key brain structures involved in the follow-up and treatment planning of vestibular schwannoma (VS): the VS and the cochleas. Currently, the diagnosis and surveillance in patients with VS are commonly performed using contrast-enhanced T1 (ceT1) MR imaging.

**BRATS 2013** [36] is a brain tumor segmentation dataset consists of synthetic and real images, where each of them is further divided into high-grade gliomas (HG) and low-grade gliomas (LG). There are 25 patients with both synthetic HG and LG images and 20 patients with real HG and 10 patients with real LG images.

**Atria 2018** [92] is a dataset of 3D Gadolinium-Enhanced Magnetic Resonance Imaging, and contains 100 Data for Training and 54 Data for Testing.

**RFMiD** [70] is a multi-label classification dataset for fundus images. The dataset contains 3200 cases and provides annotations for 45 eye diseases.



**COSMOS**<sup>7</sup> is a dataset designed to segment the blood vessel wall from the influence of 3D-VISTA and accurately diagnose atherosclerotic lesions. The dataset provides 50 cases for model training and validation, and 25 cases for testing.

**CT-ORG** [77] is a CT multi-organ segmentation dataset that officially provides annotations of 6 organs: lungs, bones, liver, kidneys, bladder, and brain, including 140 CT scans, of which 131 were directly derived from LiTS and 9 were derived from CT data from PET-CT at Harvard Medical School. Officially, the dataset is divided into 119 training sets and 21 test sets.

**PROMISE12** [53] is a classic dataset in the field of medical image segmentation, and as part of the MICCAI 2012 challenge, 50 prostate MRI images and their corresponding segmentation annotations were provided.

**TotalSegmentator** [83] is currently the largest publicly available dataset in the field of 3D medical image segmentation, including 1204 CT images covering 104 anatomical structures throughout the body. Of these, 1082 were used for training, 57 for validation, and 65 for the test set.

**BHX** [76] is a public available dataset with bounding box annotations for 5 types of acute hemorrhage as an extension of the qure.ai CQ500 dataset, containing up to 39,668 bounding boxes in 23,409 images annotated for hemorrhage, out of a total of 170k images from qure.ai CQ500 dataset.

**MSD Prostate** [78] aims to segment two regions of the prostate, the central gland and the peripheral band, from multimodal MR (T2, ADC) images. The dataset includes T2 and ADC MR images of 48 patients, which are officially divided into 32 training sets and 16 test sets.

**The Bone Marrow Cytomorphology** [60] is a dataset focused on bone marrow cell morphology, contains more than 170,000 de-identified, expert-annotated images of cells from bone marrow smears from 945 patients using May-Grünwald-Giemsa/Pappenheim staining.

**PALM19** [22] is focusing on the research and development of advanced algorithms for the diagnosis of pathological myopia (PM), as well as the accurate segmentation of lesion areas in the fundus photos of PM patients, a total of 1,200 images with detailed annotations were provided, which were divided into 400 training images, 400 validation images and 400 test images to support the algorithm development and testing of the participants.

**OmniMedVQA** [33] is collected from 73 different medical datasets, including 12 different modalities and covering more than 20 distinct anatomical regions. Importantly, all images in this benchmark are sourced from authentic medical scenarios, ensuring alignment with the requirements of the medical field and suitability for evaluating LVLMS.

**ISLES22** [32] is designed to automatically segment acute to subacute ischemic stroke lesions by multimodal MR images, including FLAIR, DWI, and ADC. The dataset brings together 400 multicenter, multi-device MRI cases that exhibit a high degree of variability in the size, number, and location of stroke lesions. The dataset is divided into a training set of 250 cases and a test set of 150 cases.

**FUMPE** [59] is a dataset for segmentation of pulmonary embolism (PE) in computed tomography (CTA) images, containing images of 35 different patients.

**MSD Cardiac** [78] aims to segment the left atrium from unimodal MR images, and the dataset includes MR images of 30 patients, which are officially divided into 20 training sets and 10 test sets.

**Med-GRIT-270k** [34] is a large-scale biomedical image-mask pairs are transformed into multi-modal conversations by leveraging chatGPT [19] in a novel process. It is the first dataset in biomedicine to integrate referring, grounding, and conversations.

**PitVis** [16] is a dataset of endoscopic pituitary surgery videos in PitVis, and provide live annotations of steps and instrument grounds, including 120024 images, and randomly divide the training set and validation set at a scale of 8:2.

**RP3D** [84] has four subsets of Caption/VQA/Rationale/Modality, which share the same data source from Radiopaedia, a medical imaging teaching website that contains 3D radiography images uploaded by doctors and descriptions.

<sup>7</sup> <https://vessel-wall-segmentation-2022.grand-challenge.org/>

**BTCV Cervix** [49] is a CT segmentation dataset for cervical cancer patients that provides radiation therapy planning, annotating 4 organs of the bladder, uterus, rectum and small intestine, containing 30 annotated training data and 20 unannotated test data.

**CMRxMotion** [82] is designed to explore cardiac MRI analysis in extreme conditions of respiratory motion. It consists of two tasks: 1) image quality evaluation and 2) segmentation. The challenge consists of 160 training sets, 40 validation sets, and 160 test sets.

**SIIM-FISABIO-RSNA COVID-19** [47] is a dataset focused on the use of advanced machine learning techniques to accurately identify and locate COVID-19 in chest radiographs. The dataset includes 6,334 high-quality chest X-rays in DICOM format.

## Test Datasets

### Visual Question Answering

**SLAKE**. Following the official split, we use 1,061 and 1,033 question-answer pairs for test on the English and Chinese version, respectively.

**VQA-RAD**. Following the official split, we use 451 question-answer pairs for evaluation.

**PathVQA**. Following the official split, we use 6,761 question-answer pairs for evaluation.

**OmnimedVQA**. We used the open access part of the OmniMedVQA dataset, which includes 42 traditional medical imaging datasets, all formatted as VQA.

**GMAI-MMbench**. The most comprehensive general medical AI benchmark with well-categorized data structure and multi-perceptual granularity to date. It contains 21,281 test data constructed from 284 datasets across 38 medical image modalities, 18 clinical-related tasks, 18 departments, and 4 perceptual granularities in a Visual Question Answering (VQA) format.

### Report Generation

**MIMIC-CXR**. Following RadFM [84], we use 4,710 cases for test.

**IU-Xray**. Following MedRegA [80], we use 1,180 cases for test.

### Medical Image Classification

**MURA**. Following the official split, we use 3,193 X-ray images for test.

**PAD-UFES-20**. Since no official split is provided, we randomly split 20% of the data for evaluation, which contains 1,044 samples.

**BRSET**. Since no official split is provided, we randomly split 20% of the data for test, which includes 3,254 fundus images.

**RFMiD 1.0**. Following the official split, we use 640 fundus images for evaluation.

**PneumoniaMNIST**. Following the official split, we use 624 X-ray samples for test.

**OrganCMNIST**. Following the official split, we use 8,216 CT samples for test.

**OrganAMNIST**. Following the official split, we use 17,778 CT samples for test.

**OrganSMNIST**. Following the official split, we use 8,827 CT samples for test.

**OCTMNIST**. Following the official split, we use 1,000 OCT scans for test.

**BreastMNIST**. Following the official split, we use 156 ultrasound scans for test.

**ChestMNIST**. Following the official split, we use 22,433 chest x-ray images for test.

**PathMNIST**. Following the official split, we use 7,179 pathology samples for test.

**VinDr-CXR**. Following the official split, we use 3,000 chest x-ray images for evaluation.

**VinDr-PCXR**. Following the official split, we use 1,387 chest x-ray images for evaluation.

**VinDr-SpineXR**. Following the official split, we use 2,077 spine x-ray images for evaluation.

**VinDr-Mammo.** Following the official split, we use 4,000 mammography images for evaluation.

### **Lesion Detection and Region Recognition**

"We evaluate our model using 1,272 test samples for region recognition and 1,000 test samples for lesion detection, each spanning 141 regions. These samples are selected from the held-out test set of the SA-Med-2D dataset. Additionally, we assess our model on the MedGRIT benchmarks, adhering to the conventions and metrics established in BiRD [34]. MedGRIT consists of four tasks: (i) Region-in and Text-out tasks, which include Referring Object Classification (ROC) with 5,293 samples and Referring Captioning (RC) with 5,265 samples; (ii) Text-in and Region-out tasks, which involve Visual Grounding (VG) with 5,276 samples; and (iii) Text-in and Text-out tasks, represented by Medical Image Analysis (MIA) with 5,293 samples.

### **External Validation**

We collected CT and MRI scans covering 11 distinct diseases across three major anatomical regions: the HEAD and NECK (including brain tumors, acoustic neuromas, and cerebral hemorrhage), CHEST (lung cancer and pulmonary embolism), and ABDOMEN (bladder, prostate, colon, liver, kidney, and pancreatic cancers). Each disease category comprises data from 20 patients, all obtained from Sun Yat-sen Memorial Hospital, Sun Yat-sen University. In total, the dataset includes 5,981 slices for external validation.

### **Prognostic Prediction**

**Lung Tumor Progression-Free Survival Prediction.** The model was trained on a multicenter dataset comprising patients from two hospitals: ZE (n = 238) and NF (n = 85). For external validation, it was evaluated on independent datasets from two additional hospitals: JX (n = 58) and HN (n = 49). During training, the data were split into an 8:2 ratio for training and internal evaluation, respectively.

**NSCLC Overall Survival Prediction.** The model was trained on the Lung1 dataset (n = 420) and externally validated on the RADIO cohort (n = 133). The training data were divided into an 8:2 ratio for training and internal evaluation.

**Glioma Tumor Overall Survival Prediction.** The model was trained on the UPENN-GBM cohort (n = 585) and externally validated on the BraTS dataset (n = 163). The training data were split into an 8:2 ratio for training and internal evaluation.

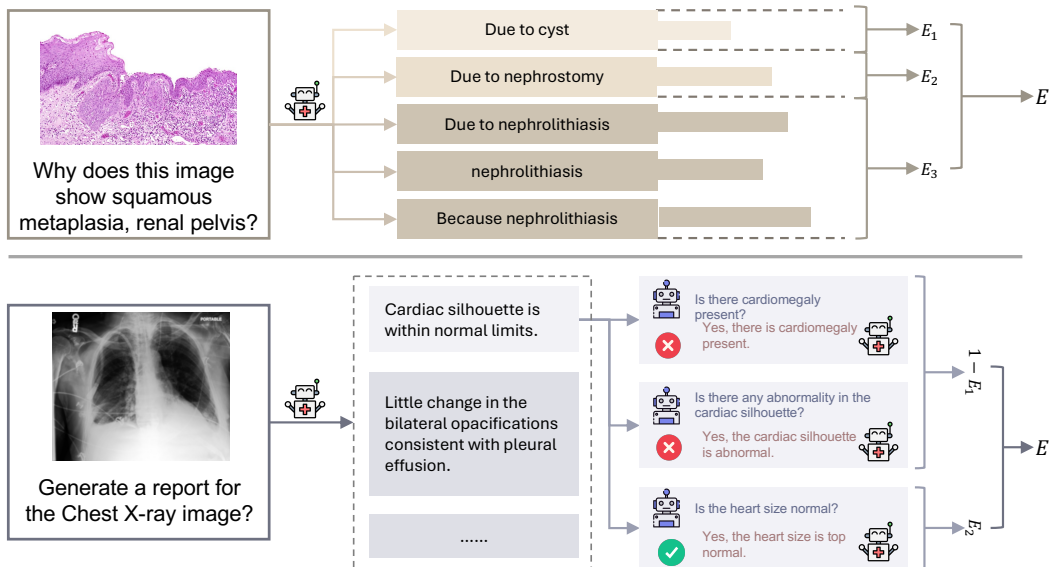


Figure 7: Overview of uncertainty estimation in visual question answering and report generation.

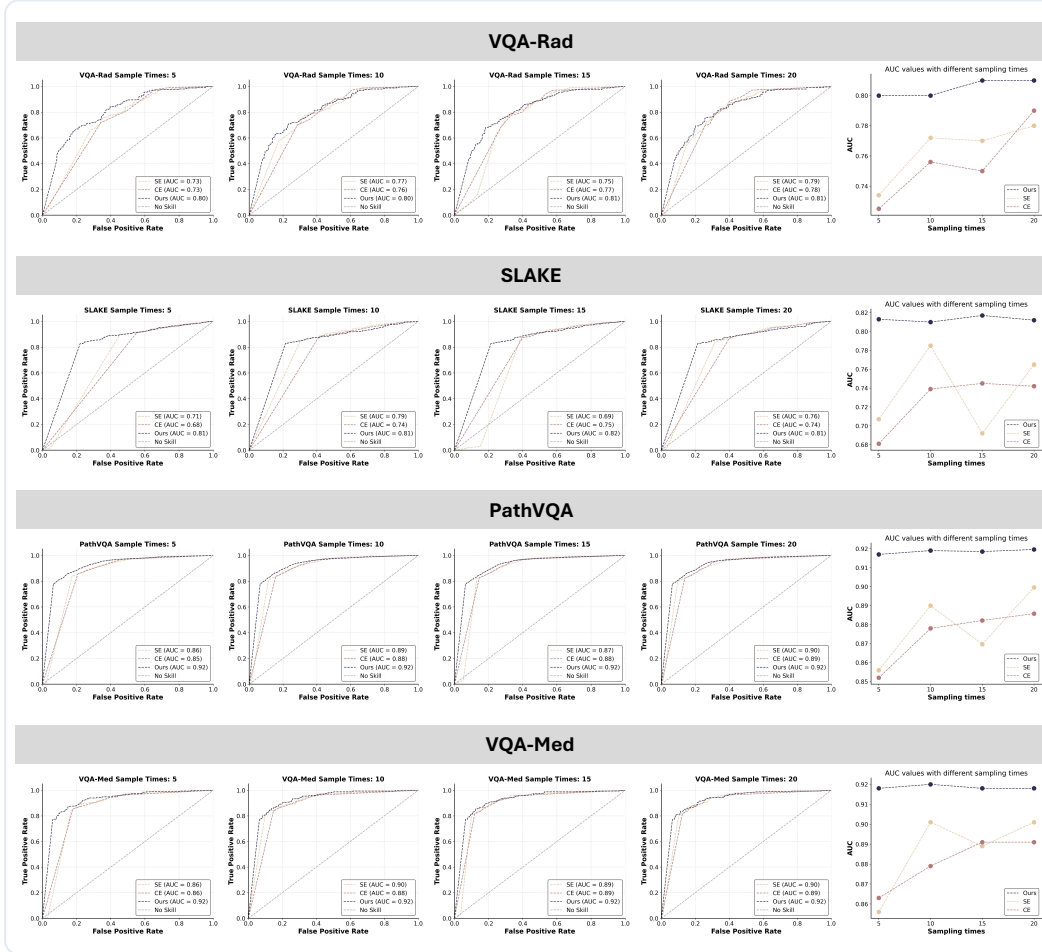


Figure 8: Ablation results on four VQA datasets demonstrating the impact of sampling frequency on uncertainty estimation. Our method consistently outperforms conventional semantic entropy, particularly when the number of sampling iterations is fewer than 10, and achieves higher AUC scores as sampling increases.



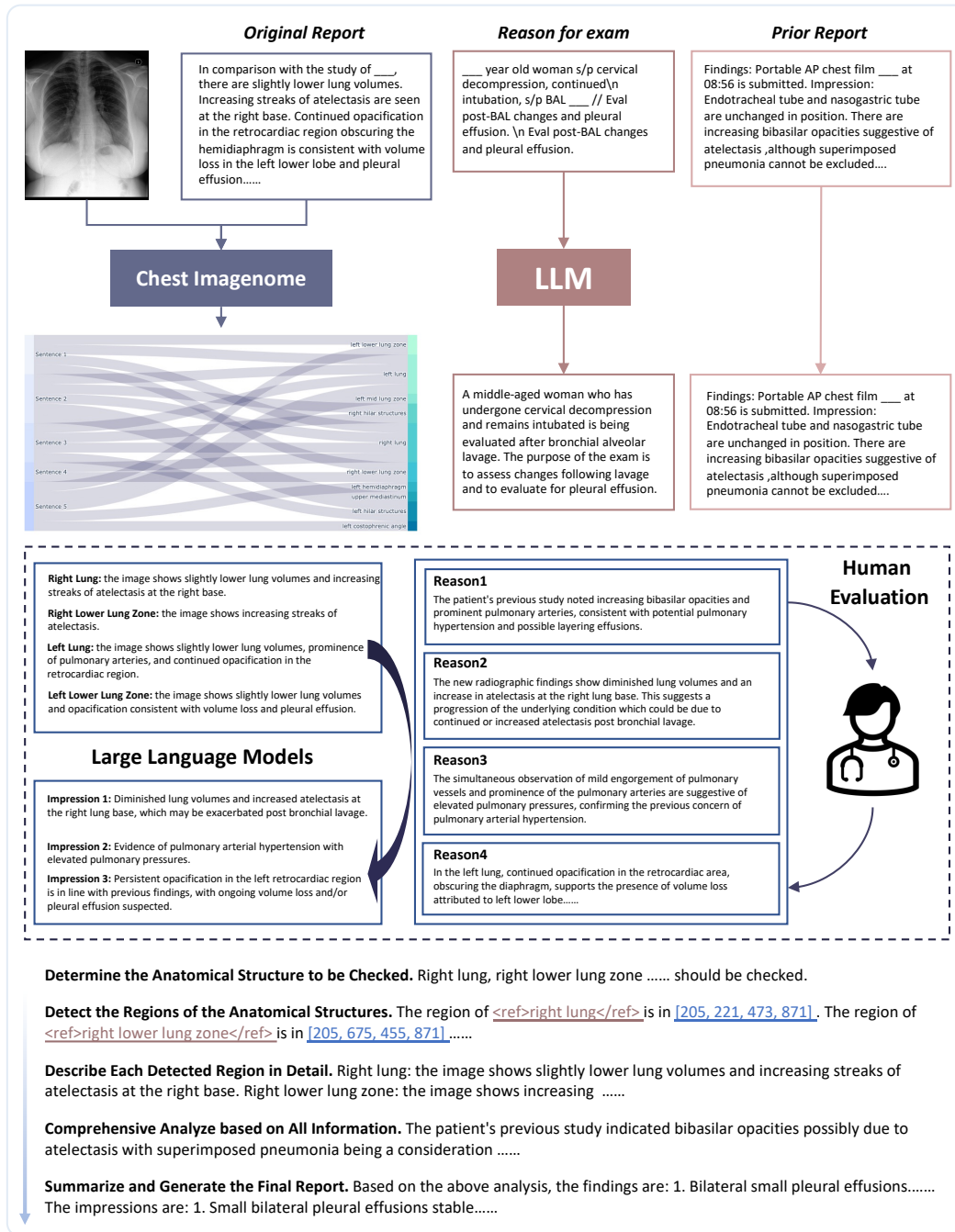


Figure 9: Schematic overview of the data curation pipeline for reasoning tasks.

### The Prompt for Lesion Detection Task

1. Can you analyze this <modality> image and identify the <class> present?
2. In this <modality> image could you detect all instances of <class>?
3. Are you capable of identifying <class> within this <modality> image?
4. Could you please detect the objects you find that belong to the <class> in this <modality> image?
5. Can you perform object detection on this <modality> image and tell me the <class> you find?
6. Can you carry out object detection on this <modality> image and identify the <class> it contains?
7. I have an <modality> image that needs examination for objects related to <class>. Can you perform that?
8. Can you determine if there are any <class> present in this <modality> image using object detection?
9. Could you help me identify the objects corresponding to <class> in the this <modality> image?
10. Are you capable of detecting and labeling <class> within this <modality> image?
11. Can you detect <class> within this <modality> image and provide information about its presence?
12. Please perform object detection on this <modality> image to identify <class>.
13. I need your expertise to locate <class> in this <modality> image.
14. Please let me know the objects falling into the <class> in this <modality> image.
15. Please help me identify objects falling under the <class> in this <modality> image.
16. Please assist me in identifying the <class> objects within this <modality> image.
17. Please analyze the <modality> image and let me know if you can find any objects categorized as <class>.
18. Please conduct object detection on the <modality> image to locate any <class> that may be present.
19. Please identify and list any <class> in the <modality> image using object detection.
20. Please analyze the <modality> image and let me know if there are any recognizable <class>.
21. Detect any <class> in this <modality> image if possible.

Figure 10: Illustration of the prompt design used for lesion detection task.

### The Prompt for Region Recognition Task

1. Here is an medical image. What is the <class> in <regions>?
2. This is an medical image. Identify the <class> in <regions>.
3. Presented is an image of <modality>. Determine the <class> in <regions>.
4. Here you see an image of <modality>. What signifies the <class> in <regions>?
5. Displayed is an image of <modality>. Identify the <class> within <regions>.
6. Look at this image of <modality>. What is the <class> found in <regions>?
7. Below is an image of <modality>. What represents the <class> in <regions>?
8. Here lies an image of <modality>. Determine the <class> in <regions>.
9. Given an image of <modality>, could you tell me what is the <class> in <regions>?
10. In the image of this <modality>, What category best describes <class> represented by <regions>?
11. Can you specify the type of <class> inside the region labeled by <regions> in the modality of <modality>?
12. How would you label <class> indicated by <regions> in this <modality>?
13. Give a label to <class> region outlined by <regions> in the <modality>.
14. Displayed is an image of <modality>. Please identify the category of the <class> inside the <regions>.
15. You are provided with an image of <modality>. Examine and determine the primary subject <class> located within <regions>.

Figure 11: Illustration of the prompt design used for region recognition task.

## The Prompt for Reasoning Data Curation

<System>

Suppose you are a radiology expert. Your task is to generate a step-by-step chain of reasoning based on the provided medical report and the patient's previous study (if exist). The report includes findings along with their corresponding regions.

Step 1: Describe each region in the provided case separately, using the descriptions from the input. Focus on one region at a time, not multiple regions together.

Step 2: Analyze how the regions and descriptions relate to the patient's information, previous study (if exist) and reason for the exam in detail. Provide a detailed reasoning path that links each finding to the corresponding impression.

Step 3: Summarize and generate the final report.

You should rephrase the indication to avoid using abbreviations or "\_". Also, you should rephrase the sentences if it contains time such as "7:10 AM". The output should be in json format as:

```
{
  "reason_for_exam": "Rephrased reason for exam"
  "Step1": "<region1>: the image shows ....\n<region2>: the image shows ...\n<region3>: the image shows ...\n...",
  "Step2": "The reasoning process with medical domain knowledge",
  "Step3": "Based on the above analysis, the findings are: 1. xxx\n2. xxx\n... The impressions are: 1. xxx\n2. xxx\n..."
}
```

</System>

<User>

"reason\_for\_exam": "\_\_\_-year-old female patient status post third renal transplant on\n \_\_\_, who presented with symptomatic cholelithiasis with increasing LFTs. \n Concern for CMV hepatitis in addition to cholelithiasis. Now with epigastric\n pain radiating to back with chest tightness, assess for volume overload.",

"patient\_info": "20-30 year old female",

"Report": {

"The pulmonary vasculature is not\n congested and there is no evidence of pleural effusion as the lateral pleural\n sinuses are free on this portable examination."

{

"region": [

"right lung", "right hilar structures", "right costophrenic angle",

"left lung", "left hilar structures", "left costophrenic angle"

]

},

.....

</User>

<Response>

``json

{

"reason\_for\_exam": "The patient is a young adult female who has undergone a third kidney transplant....."

"step1": "For the right lung and right hilar structures, the image shows that the pulmonary vasculature is not congested, and there is no evidence of pleural effusion, as the lateral pleural sinuses are free....."

"step2": "The imaging findings reveal no congestion in the pulmonary vasculature and no pleural effusion in the typical spaces, suggesting no acute volume overload in the chest....."

"step3": "The examination shows no evidence of pulmonary congestion or new infiltrates, effectively ruling out significant pulmonary volume overload as the cause of the patient's symptoms....."

}

...

</Response>

Figure 12: Illustration of the prompt design used for reasoning data curation.

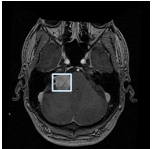
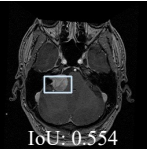
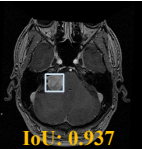
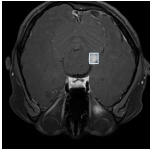
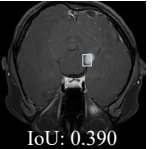
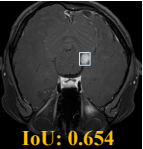
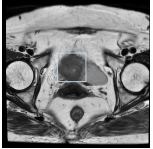
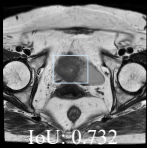
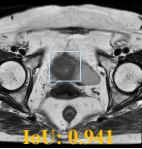
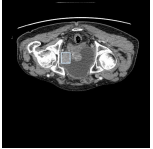
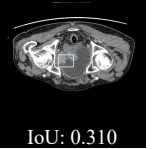
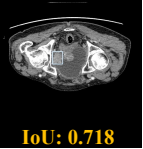
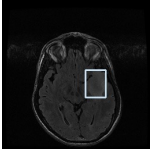
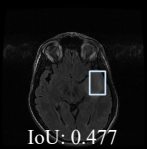
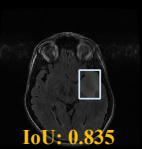
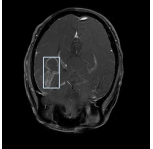
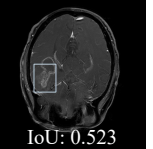
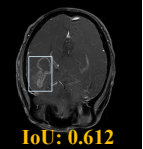
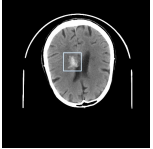
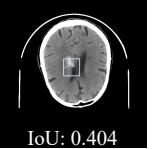
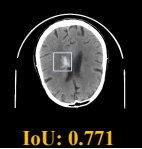
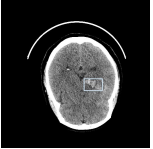
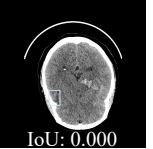
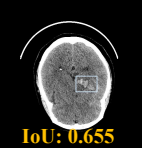
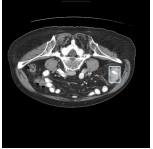
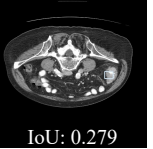

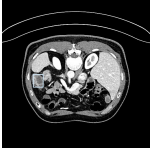
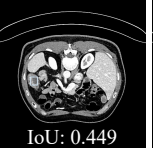
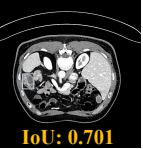

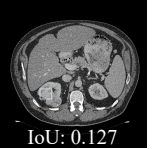
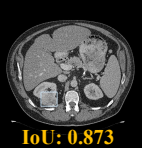
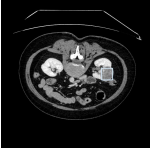
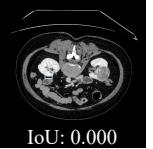
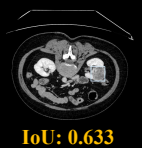

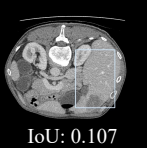
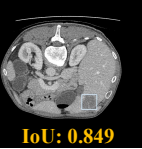
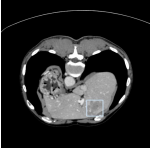
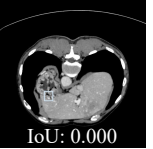
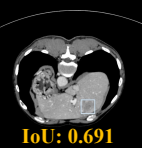
	Internal Validation			External Validation		
	Reference	MedRegA	Ours	Reference	MedRegA	Ours
Acoustic Neuroma		 IoU: 0.554	 <b>IoU: 0.937</b>		 IoU: 0.390	 <b>IoU: 0.654</b>
Bladder Cancer		 IoU: 0.732	 <b>IoU: 0.941</b>		 IoU: 0.310	 <b>IoU: 0.718</b>
Brain Tumor		 IoU: 0.477	 <b>IoU: 0.835</b>		 IoU: 0.523	 <b>IoU: 0.612</b>
Cerebral Hemorrhage		 IoU: 0.404	 <b>IoU: 0.771</b>		 IoU: 0.000	 <b>IoU: 0.655</b>
Colon Cancer		 IoU: 0.279	 <b>IoU: 0.916</b>		 IoU: 0.449	 <b>IoU: 0.701</b>
Kidney Cancer		 IoU: 0.127	 <b>IoU: 0.873</b>		 IoU: 0.000	 <b>IoU: 0.633</b>
Liver Cancer		 IoU: 0.107	 <b>IoU: 0.849</b>		 IoU: 0.000	 <b>IoU: 0.691</b>

Figure 13: Qualitative comparison between XmedGPT and a state-of-the-art Generalist Medical AI (GMAI) model on lesion detection tasks.

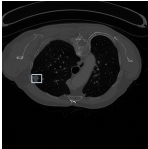
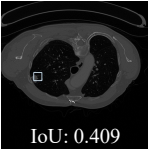
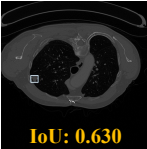
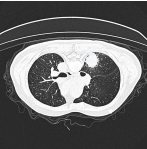
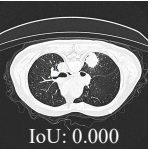
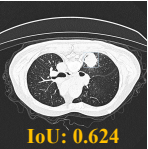
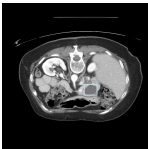
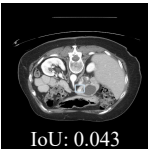
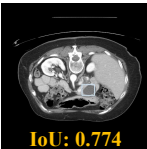
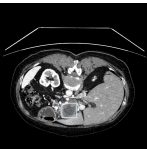
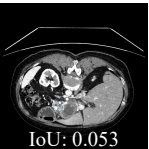
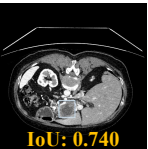
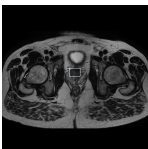
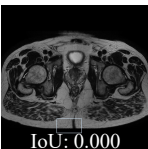
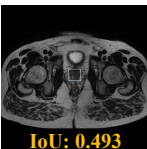
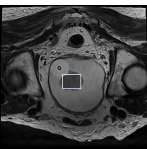
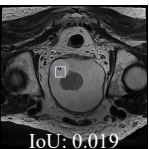
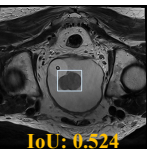




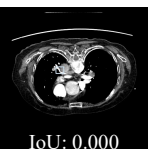
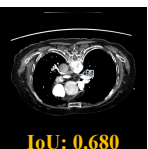
	Internal			External		
	Reference	MedRegA	Ours	Reference	MedRegA	Ours
Lung Cancer		 IoU: 0.409	 <b>IoU: 0.630</b>		 IoU: 0.000	 <b>IoU: 0.624</b>
Pancreatic Cancer		 IoU: 0.043	 <b>IoU: 0.774</b>		 IoU: 0.053	 <b>IoU: 0.740</b>
Prostatic Cancer		 IoU: 0.000	 <b>IoU: 0.493</b>		 IoU: 0.019	 <b>IoU: 0.524</b>
Pulmonary Embolism		 IoU: 0.041	 <b>IoU: 0.710</b>		 IoU: 0.000	 <b>IoU: 0.680</b>

Figure 14: Qualitative comparison between XmedGPT and a state-of-the-art Generalist Medical AI (GMAI) model on lesion detection tasks.

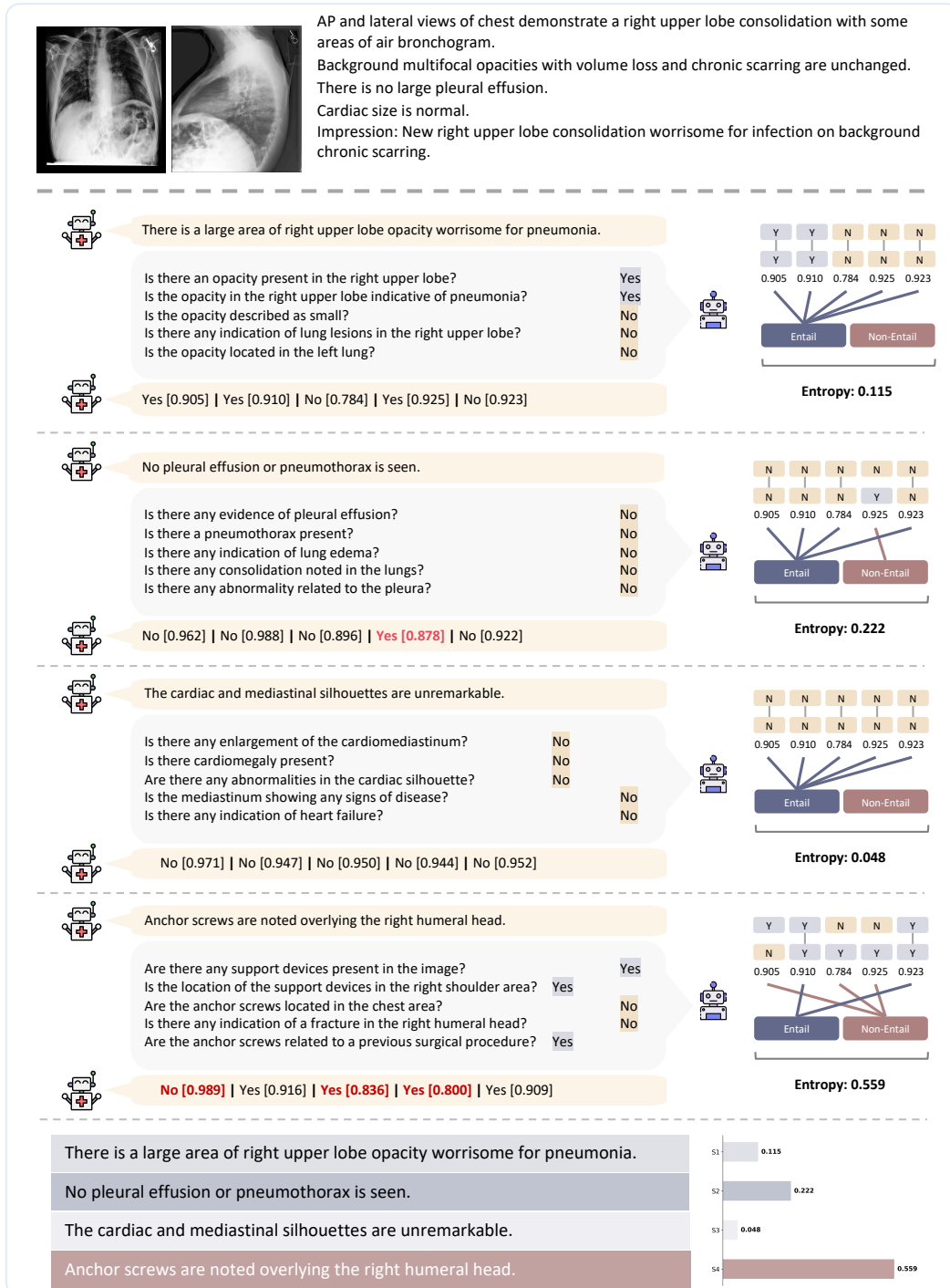
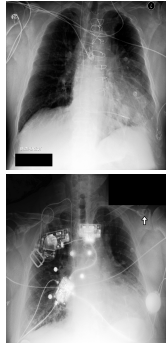


Figure 15: Representative example illustrating the uncertainty estimation pipeline and its corresponding results.





You are a radiology expert reviewing a chest X-ray study.

**Current frontal image:** <image>

**Prior frontal image:** <image>

**Prior radiology report:** findings ap view of the chest. a temporary pacemaker lead is unchanged and in appropriate position. mild cardiomegaly is unchanged. no focal consolidation pleural effusion or pneumothorax. impression temporary pacemaker lead is in appropriate position. no acute cardiopulmonary process.

**Patient information:** 50-60 year old male.

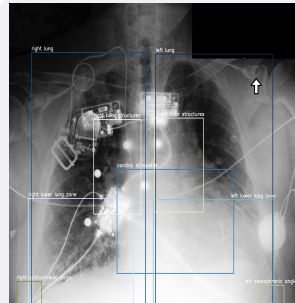
**Reason for the exam:** \_\_\_-year-old man status post cardiac arrest., provide a detailed diagnostic assessment. Clearly identify the key findings, their anatomical locations, and explain how these observations support or contradict the suspected diagnosis.



Findings: A single portable frontal upright view of the chest is provided. External pacing wires and electronics partially obscure the view. Moderate cardiomegaly is unchanged. Lung volumes have slightly increased. Mild pulmonary edema persists. There is no focal consolidation, large pleural effusion or pneumothorax. Sternotomy wires are noted. Impression: Moderate cardiomegaly and mild pulmonary edema.



Findings: As compared to the previous radiograph there is a newly appeared parenchymal opacity at the left lung base. The opacity shows air bronchograms is ill-defined and likely to reflect pneumonia. The smaller component of the opacity is located in the medial parts of the lingula. There is no reactive pleural effusion. Otherwise the lung parenchyma is unremarkable. Normal size of the cardiac silhouette. Normal hilar and mediastinal structures.



#### Describe Each Detected Region in Detail.

Right lung, right hilar structures, left lung, left hilar structures: the image shows mild pulmonary edema.

Right lung, right costophrenic angle, left lung, left costophrenic angle: the image shows no pleural effusion or pneumothorax.

Right lung, left lung, mediastinum, cardiac silhouette: the image shows no acute cardiopulmonary process.

Mediastinum, cardiac silhouette, right atrium: the image shows a right internal jugular transvenous pacer defibrillator lead ending in the right ventricle.

Cardiac silhouette: the image shows moderate cardiomegaly.



**Comprehensive Analyze based on all information.** The reasoning process begins with the observation of mild pulmonary edema in both the right and left lungs, as well as the right and left hilar structures. This finding suggests fluid accumulation in the lung tissues, which can be associated with heart failure or fluid overload. The absence of pleural effusion or pneumothorax in the right and left lungs, as well as the right and left costophrenic angles, indicates that there is no abnormal fluid collection in the pleural space or air leakage into the pleural cavity, which could complicate the patient's condition. The finding of no acute cardiopulmonary process in the right lung, left lung, mediastinum, and cardiac silhouette suggests that there is no immediate life-threatening condition affecting the heart or lungs. The presence of a right internal jugular transvenous pacer defibrillator lead ending in the right ventricle indicates that the patient has an implanted device to manage heart rhythm issues, which is consistent with the patient's history of cardiac arrest. Finally, the moderate cardiomegaly observed in the cardiac silhouette suggests an enlargement of the heart, which can be a sign of chronic heart conditions such as heart failure or long-standing hypertension.

**Summarize and Generate the Final Report.** Based on the above analysis, the findings are: 1. Mild pulmonary edema in the right and left lungs and hilar structures. 2. No pleural effusion or pneumothorax in the right and left lungs and costophrenic angles. 3. No acute cardiopulmonary process in the right and left lungs, mediastinum, and cardiac silhouette. 4. Right internal jugular transvenous pacer defibrillator lead ends in the right ventricle. 5. Moderate cardiomegaly in the cardiac silhouette. The impressions are: 1. Mild pulmonary edema. 2. No pleural effusion or pneumothorax. 3. No acute cardiopulmonary process. 4. Presence of a right internal jugular transvenous pacer defibrillator lead in the right ventricle. 5. Moderate cardiomegaly.

Figure 16: Representative example of trustworthy report generation with integrated visual and textual explainability.

Table 1: Comparison of Methods Across Medical VQA Benchmarks with Best in Bold

Dataset	Metric	RadFM	LLaVA-Med	MedFlamingo	InternVL	MedDr	MedRegA	Ours
Slake-VQA	BLEU-1	0.7522	0.6619	0.1087	0.3776	0.7648	0.8155	<b>0.8844</b>
	ClosedAcc	0.7408	0.3887	0.4648	0.1718	0.8338	0.8535	<b>0.9239</b>
	OpenRecall	0.7726	0.8155	0.2719	0.5076	0.7418	0.8045	<b>0.8774</b>
	Recall	0.7620	0.6727	0.3280	0.3953	0.7726	–	<b>0.8930</b>
	OpenAcc	0.7408	0.7819	0.2295	0.4703	0.7053	–	<b>0.8470</b>
	F1	0.7598	0.6687	0.1595	0.3871	0.7756	0.8206	<b>0.8917</b>
PathVQA	BLEU-1	0.2489	0.4479	0.1027	0.0340	0.6143	0.5952	<b>0.6280</b>
	ClosedAcc	0.4886	0.5600	0.5739	0.0307	0.9021	0.8912	<b>0.9071</b>
	OpenRecall	0.0249	<b>0.3791</b>	0.0664	0.0499	0.2800	0.3356	0.3649
	Recall	0.2570	0.4607	0.3202	0.0403	0.6192	–	<b>0.6368</b>
	OpenAcc	0.0128	<b>0.3487</b>	0.0457	0.0353	–	–	0.3282
	F1	0.2524	0.4547	0.1522	0.0384	0.6215	0.6069	<b>0.6344</b>
VQA-RAD	BLEU-1	0.4864	0.3746	0.1423	0.2626	0.5962	<b>0.6189</b>	0.6083
	ClosedAcc	0.6534	0.2231	0.4741	0.2709	0.7888	0.7530	<b>0.8048</b>
	OpenRecall	0.3683	<b>0.6335</b>	0.2573	0.3408	0.3745	0.4603	0.4507
	Recall	0.5270	0.3851	0.3758	0.3019	0.6051	–	<b>0.6478</b>
	OpenAcc	0.3150	<b>0.5950</b>	0.1800	0.2750	0.3000	–	0.3500
	F1	0.5005	0.3838	0.1998	0.2777	0.6110	0.6224	<b>0.6282</b>

Table 2: Performance Comparison on Single-Label and Multi-Label Benchmarks with Best in Bold

Category	Dataset	RadFM	LLaVA-Med	MedFlamingo	InternVL	MedDr	MedRegA	Ours
Single-Label	OrganAMNIST	0.0123	0.1490	0.0478	0.0891	0.2066	0.2937	<b>0.9356</b>
	OrganCMNIST	0.0662	0.0750	0.0149	0.0462	0.0699	0.2422	<b>0.8546</b>
	OrganSMNIST	0.0649	0.0727	0.0132	0.0467	0.0868	0.1898	<b>0.7138</b>
	PathMNIST	–	0.0834	–	0.0685	0.2306	–	<b>0.9556</b>
	OCTMNIST	0.1997	0.1305	0.1000	0.0929	0.5831	0.6446	<b>0.8834</b>
	PneumoniaMNIST	0.5865	0.5000	0.7131	0.2359	0.8734	0.8523	<b>0.9400</b>
	BreastMNIST	0.3526	0.3782	0.3077	0.0640	0.7179	0.7035	<b>0.8329</b>
	PAD-UFES-20	0.1381	0.1290	0.0259	0.0220	0.1409	0.2024	<b>0.4746</b>
	MURA	0.4950	0.3631	0.3430	0.0154	0.3781	0.6999	<b>0.7938</b>
Multi-Label	ChestMNIST	0.0491	–	–	–	0.1339	0.1196	<b>0.2386</b>
	VinDr-CXR	0.0657	0.0236	0.0159	0.0225	0.0711	0.1189	<b>0.3423</b>
	VinDr-PCXR	0.0808	0.0192	0.0231	0.0220	0.0817	0.0633	<b>0.1122</b>
	VinDr-SpineXR	0.1667	0.0249	0.0847	0.0817	0.2682	0.3016	<b>0.3852</b>
	VinDr-Mammo	0.1389	0.0325	0.0085	0.0154	0.1935	0.0999	<b>0.1621</b>
	RFMiD	0.0554	0.0265	0.0153	0.0225	0.0189	0.0655	<b>0.2160</b>
	BRSET	0.0676	0.0793	0.0248	0.0817	0.0249	0.1128	<b>0.3786</b>

Table 3: Performance Comparison on Medical Report Generation Benchmarks with Best in Bold

Dataset	Metric	RadFM	LLaVA-Med	MedFlamingo	InternVL	MedDr	MedRegA	Ours
MIMIC-CXR	BLEU-4	0.0555	0.0096	0.0191	0.0133	0.0759	<b>0.1030</b>	0.0929
	ROUGE-L	0.2052	0.1390	0.1460	0.1250	0.2259	0.2440	<b>0.2528</b>
	CheXbert-F1@Pos	–	–	–	0.2770	0.1030	0.4190	<b>0.4790</b>
IU-Xray	BLEU-4	0.1028	0.0068	0.0206	0.0156	0.1222	<b>0.1480</b>	0.1455
	ROUGE-L	0.2607	0.0996	0.1111	0.1218	0.2835	0.3040	<b>0.3335</b>
	CheXbert-F1@Pos	–	–	–	0.2160	0.5647	0.5440	<b>0.5690</b>

Table 4: Performance Comparison on GMAI-MMBench with Best in Bold

Category	Task	GPT-4O	LLaVA-Med	MedFlamingo	InternVL	MedDr	MedRegA	Ours
GMAI	Overall	0.5396	0.1960	0.1164	0.4360	0.4369	0.4422	<b>0.6460</b>
	Attribute Recognition	0.3832	0.2451	0.0667	0.5111	0.4120	0.3556	<b>0.8755</b>
	Blood Vessels Recognition	0.6101	0.1783	0.1014	0.4593	0.5070	0.4444	<b>0.7743</b>
	Bone	0.5708	0.1708	0.0923	0.3771	0.3785	0.5371	<b>0.8827</b>
	Cell Recognition	<b>0.4902</b>	0.1986	0.1127	0.4609	0.2987	0.3043	0.4492
	Counting	0.4662	0.1504	0.0662	0.3511	0.2827	0.2872	<b>0.6346</b>
	Disease Diagnosis	0.6145	0.1981	0.1343	0.5019	<b>0.5253</b>	0.5184	0.6530
	Image Quality Grading	0.4656	0.2024	0.1215	0.3600	0.3603	0.3200	<b>0.7320</b>
	Microorganism Recognition	0.5638	0.2151	0.0638	0.5481	0.3145	0.4593	<b>0.8131</b>
	Muscle	0.3400	0.1320	0.0800	0.2400	0.296	0.3800	<b>0.6000</b>
	Nervous Tissue	<b>0.7525</b>	0.1515	0.1818	0.625	0.4747	0.5250	0.6700
	Organ Recognition - Abdomen	0.5379	0.2042	0.0926	0.3061	0.3337	0.4286	<b>0.6509</b>
	Organ Recognition - Head & Neck	0.6947	0.2373	0.1827	0.4581	0.5133	0.5226	<b>0.7329</b>
	Organ Recognition - Pelvic	0.4867	0.1767	0.1100	0.4400	0.3267	0.2533	<b>0.5333</b>
	Organ Recognition - Thorax	0.6588	0.1965	0.1153	0.3882	0.4447	0.3882	<b>0.7624</b>
	Severity Grading	0.3393	0.2170	0.1216	0.3631	0.3514	0.3690	<b>0.3847</b>
	Surgeon Action Recognition	0.2288	0.1981	0.0519	0.2522	0.2519	0.2435	<b>0.7154</b>
	Surgical Instrument Recognition	0.2951	0.1411	0.0847	0.2510	0.2558	0.2510	<b>0.4076</b>
	Surgical Workflow Recognition	0.3943	0.2086	0.1143	0.2571	0.3229	0.2857	<b>0.5428</b>

Table 5: Performance on OmniMedVQA Benchmark with Best in Bold with Best in Bold

Category	Modality	RadFM	LLaVA-Med	MedFlamingo	InternVL	MedDr	MedRegA	Ours
OmniMedVQA	CT	0.3330	0.2530	0.3460	0.5963	0.6934	0.6564	<b>0.8251</b>
	Fundus Photography	0.3500	0.4840	0.3330	0.7638	0.7501	0.7977	<b>0.8099</b>
	MRI	0.2200	0.3590	0.2750	0.7338	<b>0.8162</b>	0.7050	0.7866
	OCT	0.3130	0.4210	0.2600	0.7548	<b>0.9139</b>	0.8506	0.8450
	Dermatoscopy	0.3630	0.4520	0.2830	0.7289	0.7224	0.7898	<b>0.8913</b>
	Microscopy	0.2800	0.4400	0.2810	0.7761	0.6409	0.7125	<b>0.8234</b>
	X-Ray	0.3150	0.3170	0.3010	0.8305	0.7900	0.7835	<b>0.9142</b>
	Ultrasound	0.2610	<b>0.8370</b>	0.3320	0.6163	0.4177	0.4661	0.8264

Table 6: Performance on Region Recognition and Lesion Detection Tasks with Best in Bold

Task	Metric	MedRegA	InternVL	Ours
Region Recognition	Head and Neck	0.4972	0.1340	<b>0.7327</b>
	Chest	0.3487	0.0460	<b>0.7186</b>
	Abdomen	0.4528	0.0720	<b>0.7273</b>
	Skeleton	<b>0.5921</b>	0.0000	0.4713
	Pathology	0.2222	0.0000	<b>0.4828</b>
	Overall	0.4226	0.0504	<b>0.6265</b>
Lesion Detection	Head and Neck	0.4378	—	<b>0.9777</b>
	Chest	0.3581	—	<b>0.9419</b>
	Abdomen	0.4664	—	<b>0.8792</b>
	Skeleton	0.3103	—	<b>0.9013</b>
	Pathology	0.1121	—	<b>0.8095</b>
	Overall	0.3369	—	<b>0.9019</b>

Table 7: Performance on MedGRIT Region VQA Benchmark with Best in Bold

Task	SubTask	BiRD	LLaVA	MedRegA	InternVL	Ours
Region VQA	VG	0.5392	0.0000	0.0000	0.0000	<b>0.7411</b>
	ROC	0.6533	0.0275	0.0724	0.1341	<b>0.8857</b>
	RC	0.5523	0.0818	0.0569	0.1065	<b>0.6908</b>
	MIA	0.5217	0.1120	0.0671	0.0565	<b>0.6156</b>

Table 8: Audio-Input Evaluation Results Across Diverse Benchmarks with Best in Bold

Task	Dataset	Intern_omni	Ours_audio	Ours_text
VQA	Slake	0.4680	0.6700	<b>0.8917</b>
	VQA-Rad	0.4350	0.4820	<b>0.6282</b>
	PathVQA	0.2690	0.5230	<b>0.6344</b>
Multi-label Diagnosis	VinDr-CXR	0.0430	0.2460	<b>0.3423</b>
	VinDr-PCXR	0.0210	0.0840	<b>0.1122</b>
	VinDr-SpineXR	0.0440	0.3640	<b>0.3852</b>
	VinDr-Mammo	0.0140	0.1300	<b>0.1621</b>
Single-label Diagnosis	OrganAMNIST	0.0680	<b>0.9400</b>	0.9356
	OrganCMNIST	0.0250	<b>0.9000</b>	0.8546
	OrganSMNIST	0.0210	<b>0.7490</b>	0.7138
	BloodMNIST	0.0800	0.6030	<b>0.8329</b>
	BreastMNIST	0.1020	0.6930	<b>0.8329</b>

Table 9: Comparison of Region Recognition and Lesion Detection on Internal vs External Test Sets with Best in Bold

Disease	Task	Internal	External
Brain Tumor	Region Recognition	<b>0.9990</b>	0.7150
	Lesion Detection	<b>0.7970</b>	0.6560
Acoustic Neuroma	Region Recognition	<b>0.9990</b>	0.8860
	Lesion Detection	<b>0.8480</b>	0.6290
Cerebral Hemorrhage	Region Recognition	0.9300	<b>0.9990</b>
	Lesion Detection	<b>0.6710</b>	0.4980
Lung Cancer	Region Recognition	<b>0.9990</b>	0.9810
	Lesion Detection	<b>0.6340</b>	0.3710
Pulmonary Embolism	Region Recognition	<b>0.9990</b>	0.9490
	Lesion Detection	<b>0.5240</b>	0.0850
Liver Cancer	Region Recognition	<b>0.9960</b>	0.9800
	Lesion Detection	0.4470	<b>0.4880</b>
Pancreatic Cancer	Region Recognition	0.9360	<b>0.9560</b>
	Lesion Detection	<b>0.5540</b>	0.4120
Kidney Cancer	Region Recognition	<b>0.9760</b>	0.6390
	Lesion Detection	<b>0.7800</b>	0.5480
Colon Cancer	Region Recognition	<b>0.1540</b>	0.1070
	Lesion Detection	<b>0.6880</b>	0.4240
Prostatic Cancer	Region Recognition	<b>0.8700</b>	0.4520
	Lesion Detection	<b>0.3760</b>	0.1520
Bladder Cancer	Region Recognition	<b>0.9600</b>	0.7890
	Lesion Detection	<b>0.5150</b>	0.4740

Table 10: Region VQA external validation results. Scores represent *mean  $\pm$  standard deviation* across four evaluation metrics rated by large language models (GPT-4o). All metrics are scored out of 10, with higher values indicating better performance.

Metric	MedDr	MedRegA	LLaVA-Med	MedFlamingo	RadFM	Ours
Consistency	6.82 $\pm$ 1.64	8.11 $\pm$ 1.35	8.01 $\pm$ 1.54	3.20 $\pm$ 1.23	4.72 $\pm$ 2.17	<b>8.67 <math>\pm</math> 0.65</b>
Clinical Relevance	6.56 $\pm$ 1.60	7.76 $\pm$ 1.20	7.83 $\pm$ 1.35	3.05 $\pm$ 1.21	4.55 $\pm$ 2.18	<b>8.50 <math>\pm</math> 0.59</b>
Accuracy	6.66 $\pm$ 1.74	8.07 $\pm$ 1.41	7.82 $\pm$ 1.66	3.42 $\pm$ 1.32	4.46 $\pm$ 2.23	<b>8.65 <math>\pm</math> 0.68</b>
Mean	7.98 $\pm$ 1.29	6.68 $\pm$ 1.64	7.89 $\pm$ 1.49	3.22 $\pm$ 1.21	4.58 $\pm$ 2.18	<b>8.61 <math>\pm</math> 0.60</b>